12-2010

Modeling and Simulation of Tunable Photonic Crystals

Weiqing Yang
University of Nebraska - Lincoln, avemax@huskers.unl.edu

MODELING AND SIMULATION OF TUNABLE PHOTONIC CRYSTALS

By

Weiqing Yang

A Thesis

Presented to the Faculty of

The Graduate College at the University of Nebraska

In Partial Fulfillment of Requirements

For the Degree of Master of Science

Major: Electrical Engineering

Under the Supervision of Professor Yongfeng Lu

Lincoln, Nebraska

December, 2010

MODELING AND SIMULATION OF TUNABLE PHOTONIC CRYSTALS

Weiqing Yang, M.S.

University of Nebraska, 2010

Advisor: Yongfeng Lu

Photonic crystals (PhCs) have wavelength scale periodically alternating refractive indexes. Photon in such structures is subject to strong scattering, experiencing distinctive redistribution of energy, yielding interesting properties such as photonic band gaps, field enhancement, strong nonlinear optic effects and photon confinement. The modified fields also alter the propagation of light beams. By proper setup, super collimation could be realized in PhCs where beams can travel long distance without spreading, while no waveguide structure is used. Redirection of light can extend the refraction to negative range, without violating physics rules. This distinguished phenomenon has been envisioned as the core mechanism for super lens to enable sub-wavelength focusing and imaging.

The objective of this work is to theoretically model and analyze both two dimensional and three dimensional photonic crystals, *esp*. with anisotropic optical materials. Attention has been focused on developing of mathematical treatment for calculating the dispersive relationship and density of states. The plane wave expansion method is employed as an analysis tool.

In two dimensional photonic band gap structures, the tunable character is realized by infiltration of liquid crystal. A uniaxial crystal model is employed in the calculation. The first part deals with the design of a refraction tuning functionality. Choosing of lattice and structure parameters is discussed. The scheme is simulated with frequency difference time domain (FDTD) method. The second part lays more emphasis on the role of anisotropy introduced in the dispersive relationship and local density of states, by in-plane directional tuning.

The complicacy of three dimensional photonic crystals poses large barrier for straightforward appreciation. An analytical method is demonstrated for identification of refraction. The tool is implemented in the following investigation of three dimensional tunable structures. The effective refractive index is thereby obtained. The tuning of dispersion relationship is visualized.

Acknowledgements

Foremost, I would like to express my deep and sincere gratitude to my advisor, Professor Yongfeng Lu, whose academic experience and hard working attitude have been of great value to me. His patience and kindness reached me through his understanding and encouraging guidance.

I wish to express my warm and sincere thanks to my committee members, Professor Dennis R. Alexander and Professor Ming Han, for their detailed and constructive comments, and important support throughout this work.

I owe my most sincere gratitude to Dr. Hao Wang, who gave me the opportunity to work with her and gave me untiring help during my whole research here. I would like to acknowledge her contribution on the experimental support of this project, with her excellent engineering skills and rich material experience.

I would like particularly to acknowledge the contribution of Dr. Zhenyu Yang and Dr. Changbao Ma. They have provided convenient access and expertise on simulation work.

I want to specially thank Dr. Hao Wang, Dr. Yunshen Zhou and Dr. Yaoxuan Han for lending untiring help and support during my difficult moments. My sincere thanks also go to all my colleagues in the Laser-Assisted Nano-Engineering Lab. Thank you for your all time companion and support.

And to my family, whom I love best, to them I can say least. Thank you.

TABLE OF CONTENT

LIST OF FIGURES

NOMENCLATURE

a	lattice constant
$\boldsymbol{B}$	magnetic field
c	light speed in vacuum
$\boldsymbol{D}$	electric displacement field
$\boldsymbol{E}$	electric field
$\boldsymbol{G}$	reciprocal lattice vector
$\boldsymbol{H}$	magnetizing field
h	magnitude of magnetizing field
i	imaginary unit
$\boldsymbol{J}$	free current
$\boldsymbol{k}$, k	wave vector
l	index for the two polarizations
n	refractive index
$\boldsymbol{Q}$	matrix for the rotation operator
r	radius of a sphere or a circle
$\boldsymbol{R}$	real lattice vector
t	time
$^{\boldsymbol{T}}$	transpose operation superscript
$\boldsymbol{v}_{\mathrm{g}}$	group velocity
$\boldsymbol{x}$	location in real space
x,y,z	Cartesian coordinates
ε	dielectric permittivity
η	density of free charge
θ	incident angle
ρ	density of states
$\boldsymbol{\sigma}$	unit field vector
ω	circular frequency
(')	(apostrophe superscript) indicator of another set of a variable of one kind

CHAPTER 1

INTRODUCTION

1.1 Background and Motivation

The wave behavior in periodic structures has been of particular interest since the advent of Bloch wave theory. In his book of '*wave propagation in periodic structures*', Léon Brillouin systematically analyzed their distinctive characters [1]. Much different from the transmission in homogenous media, the destructive and constructive superposition caused by periodic scattering leads the dispersion diagram to disconnected bands. The frequency disconnection locating around the boundaries of Brillouin zones are pictorially termed as band gaps, implying the wave within the frequency range cannot propagate in the structure. The theory was applied successfully in describing the phononic and electronic systems, unprecedentedly unraveled many puzzles. In electronic systems, it has largely unveiled the mechanism of conductors, insulators and semiconductors. The triumph is not only celebrated in electronic materials. The Bloch theory concepts found their counterparts in analyzing electromagnetic waves. The frequency windows in which no mode of light could be supported is accordingly termed as photonic band gaps (PBGs). Structures with complete, incomplete and no band gap are the analogy of insulators, semiconductors and conductors. The idea of manipulating photon as electron has been of great attraction. What makes it even fascinating is, in electronic systems, the many-body interaction is inevitable. Therefore the strict solution to a system is often subject to its complexity, and usually approximation has to be introduced. While for photon system, the interaction is usually negligible, hence strict mathematical treatment are relatively easier and more desirable, which in turn greatly lowers the barrier for designing

structures with novel functionality. As for the practical application, no interaction implies the photonic device could have robust performance.

With this in mind, the photonic crystals (PhCs) have triggered intensive and extensive research interests, since Yablonovitch coined the term photonic crystal around two decades ago [2]. Great efforts have been spent on developing functional structures and devices for confining, guiding, and coupling light in sub-wavelength scale, aiming at versatile applications. Innovations have been made in developing PhC lasers, PhC optic fibers, micro cavities, high effect light emission diodes, performance enhanced solar cells and many advanced components for optical communication, such as polarization splitters, switches, multiplexers, *etc*. With the help of PhCs, devices could advance to a new level in terms of compactness, performance and reliability. In the mean time, the rich physics underlying these functionalities has become a great part of the hot topics in modern physics, such as negative refraction, super collimation, high harmonica generation, defect modes, disorder structures, optical localization, optical soliton, ultrafast phenomena, near field effects, and quantum optics, *etc*. To some extent, the floodgate holding the next generation photon based science and technology has been opened.

On the other hand, it is highly desirable to realize real-time and on-demand tunability of PhCs for applications in optical devices, such as switches, sensors, lasers and displays. Liquid crystals and dyes have been proposed to infiltrate in

the PhCs, where temperature and/or electro-optical tuning is applied [3,4]. Ferromagnetic materials have also been discussed, with the change of external magnetic field [5,6]. Schemes based on structure controlling are recently proposed, either by mechanical force, named mechanically tunable PhC (MTPC) [7], or by soft polymeric materials which are sensitive to pH value and/or temperature [8,9,10]. In this work, the nematic liquid crystal is proposed as infiltration in the photonic band gap structures. External electric field is applied to modulate the orientation and alignment of the liquid crystal molecules.

It is essential to get an understanding of light propagation and field distribution in PhCs, to efficiently and systematically design and implement these structures. The main goal of this research is to develop efficient theoretical analysis procedures. A general method based on the plane wave expansion (PWE) theory is introduced to predict the light refraction and transmission. Comparing with the popular finite difference time domain simulation (FDTD), it excels in significantly reduced memory and computation cost. The tuning effects are analyzed, and a refraction controlling scheme is theoretically demonstrated.

1.2 Thesis Outline

The work is arranged as follows. The background and motivation are briefly stated in Chapter One, along with the outline. In Chapter Two, several aspects about the PhCs are introduced, including the definition, fabrication method, and a general description of the PWE method. Modeling of anisotropy is discussed in

Chapter Three. This part focuses on the tuning effect in two dimensional structures. Design of refraction tuning is achieved and demonstrated. The anisotropy is considered in a full three dimensional model in Chapter Four, with emphasis on refraction analysis. Concluding remarks are made in Chapter Five.

References

[1] L. Brillouin, *Wave propagation in periodic structures*, Dover Pubns, 2003.

[2] E. Yablonovitch, "Inhibited spontaneous emission in solid-state physics and electronics," *Physical review letters*, vol. 58, 1987, p. 2059–2062.

[3] S. Leonard, J. Mondia, H. van Driel, O. Toader, S. John, K. Busch, A. Birner, U. Gösele, and V. Lehmann, "Tunable two-dimensional photonic crystals using liquid crystal infiltration," *Physical Review B*, vol. 61, 2000, pp. R2389-R2392.

[4] K. Busch and S. John, "Liquid-Crystal Photonic-Band-Gap Materials: The Tunable Electromagnetic Vacuum," *Physical Review Letters*, vol. 83, 1999, pp. 967-970.

[5] N. Yamamoto, S. Noda, and A. Sasaki, "New realization method for three-dimensional photonic crystal in the optical wavelength region: Experimental Consideration," *Jpn. J. Appi. Phys. Vol*, 1997.

[6] J. Wijnhoven and W. Vos, "Preparation of photonic crystals made of air spheres in titania," *Science*, 1998.

[7] W. Park and J. Lee, "Mechanically Tunable Photonic Crystals," *Optics and Photonics News*, vol. 20, 2009, p. 40.

[8] M. Honda, T. Seki, and Y. Takeoka, "Dual Tuning of the Photonic Band-Gap Structure in Soft Photonic Crystals," *Advanced Materials*, vol. 21, 2009, pp. 1801-1804.

[9] X. Xu, A.V. Goponenko, and S.A. Asher, "Polymerized PolyHEMA photonic crystals: pH and ethanol sensor materials," *Journal of the American Chemical Society*, vol. 130, 2008, pp. 3113-9.

[10] A.C. Arsenault, D.P. Puzzo, I. Manners, and G.A. Ozin, "Photonic-crystal full-colour displays," *Nature Photonics*, vol. 1, 2007, pp. 468-472.

CHAPTER 2

BACKGROUND

2.1 Definition of Photonic Crystals

PhCs are structures consisting of periodically varied materials, which thereby modulate the light wave by interaction with its electric and/or magnetic field. In most situations the media vary in dielectric permittivity because the permeability for general optical materials is usually small in difference, and the magnetic effect is often negligible comparing with the electric effect. Though, in some cases, the permeability is considered as dealing with magneto-optic materials [1-3]. The term, crystal, is an analogy to electronic materials, to show they have a resemblance in lattice structures. The lattice may repeat itself in one dimension, two dimensions or three dimensions, and PhCs are categorized accordingly.

A stack of alternating layers of two or more different materials can be regarded as 1D PhC, which is also termed as super lattice. A Bragg mirror is a case of such kind. In Fig. 2.1(a), alternatively in the horizontal direction, two different layers pictured in black and white repeat themselves, which are of dielectric constants ε_1 and ε_2, with thickness of d_1 and d_2, respectively. A two-layer-pair forms a unit cell, with the lattice constant $a = d_1 + d_2$. The effect of such device can be simply explained by interference of incident and reflective waves on each interface. For particular range of wave length, the destructive superposition inside the device eliminates the wave field. The structure then blocks the transmission, in other words, it appears highly reflective to the incidence. Detailed analysis gives its dispersive relation as shown in Fig. 2.1(b).

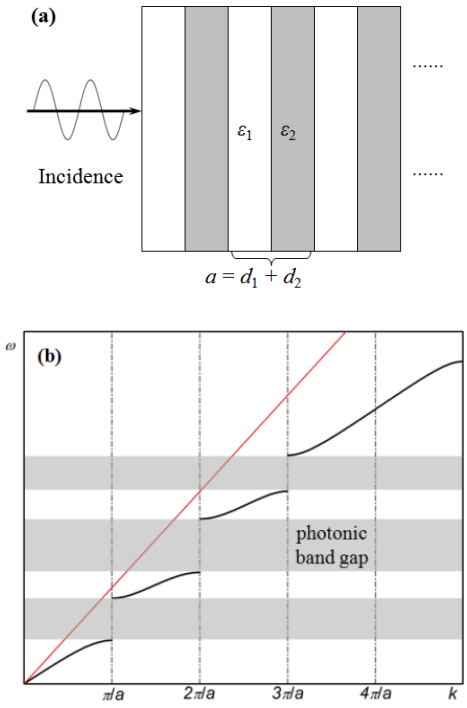

Figure 2.1 (a) A Bragg mirror composed of two alternatively arranged media, and its (b) dispersive relationship diagram. Band gaps are located on the boundaries of Brillouin zones. The red straight line indicates the dispersion relationship in otherwise a homogenous medium.

Comparing with the dispersion relation in a homogenous medium, the diagram is no longer a straight line. Frequency gaps open up when the wave vectors meet the condition $k = n\pi/a$. Continuous segments between these locations form photonic bands. These particular $\boldsymbol{k}$ points are the boundaries of Brillouin zones. Within the frequency gaps, there is no optical mode supporting the propagation light. For this reason the PhCs are also called photonic band gap structures. The existence of band gaps makes the PhCs perfect reflectors for light with corresponding frequencies. On the other hand, by introducing defects into the elsewhere perfect lattice, defect modes can be created within the band gaps. For these modes, light

waves are tightly confined in the vicinity of the defects, *i.e*. the modes are localized, enabling straightforward applications including high Q cavities and waveguides [2-8]. Further, the confinement and concentration of optical field in a sub-wavelength scale prompts the enhancement of nonlinear effects, spontaneous emission [9-17].

It is well established that the characteristics of photonic structures and composite materials are readily reflected in the band diagram. Such characteristics include the types of lattice symmetry, dielectric permittivity contrasts of the composite materials, filling factor (volume ratio) of each primitive cell, and other topological factors of the building blocks of the structure's unit cell.

One of the most important characters of the propagation of light in a dispersive medium is the speed of propagation, which is defined as group velocity,

$$\boldsymbol{v}_g \equiv \nabla_{\boldsymbol{k}}\omega \tag{2.1}$$

where v_g is the group velocity, and ω is the frequency, a function of wave vector $\boldsymbol{k}$. In the band diagram of one-dimensional PhCs, the definition could be geometrically regarded as the slope of the dispersive curves. For homogenous medium, it is invariant, standing for a constant propagation speed. While the case in band gap structures turns out much different. Particularly, the diagram flattens in the proximity of Brillouin zone boundaries, in the mean time, forming a ceiling or floor of a band, called the band edge. According to (2.1), the wave propagation slows down and tends to freeze. Slow and ultra slow light have been intensively

studied, and numerous practical applications have been proposed. The slowed propagation allows the realization of delay lines, optical memory, and buffers for light signals. Optical devices also benefit from the spatial concentration to be made in more compact size. The light-matter interactions can be enhanced owing to the accumulation of field intensity, such as nonlinearity, optical absorption, gain, and magnetic Faraday rotation, *etc.* [17,18].

The resemblance of band diagram between photonic crystals and electron materials suggests they share similarity in concepts and mathematic methodology of treating the two categories. Though, the differences should be noticed that make PhCs distinctive. Firstly, the electron is not massless as photon does. The dispersion relationship for a free electron is parabolic rather than linear for light. Second, the quantum wave function of electron is scalar, while for light wave both electric and magnetic fields are vectorial. The extra spatial dimensions combined with the correlation between the two fields, multiplies the difficulty of the mathematical treating of PBG structures. Polarization becomes a key factor to describe such a system. Thirdly, the coupling and interaction among many electrons are so complicated that the exact solution for an electron system is hardly desirable. Approximation to both modeling and solving the problem is inevitable. On the contrary, here lies the beauty of photonic systems. In general cases, it is safe to deem photon as interaction free. Therefore, exact mathematic solution could be desirable, and the power of computer simulation can be employed confidently without the concern of interaction. Another privilege the

PhCs analysis enjoys is that the master equation is scale invariant. For this reason, the band diagram remains the same shape despite the simultaneous varying of the covariant structure size and the wavelength of the light mode. Great convenience is thus endowed for designing and analyzing PhCs for on demand application with specified wavelength. In contrast, the mass of electron changes this fascinating property, as a result electron systems are usually studied case by case.

2.2 Aspect of Fabrication

Naturally occurring PBG structures have long been attracting people before the term of PhC was brought up. Such delicate structures underlie many beautiful insects appearance, such as the dazzling wings of butterflies and the shells of beetles. Several kinds of sea algae also have developed layers of such structure on their leaves to shield off the damaging ultraviolet rays. In the inorganic world, nacre and opal are of such kind possessing the periodic structures in wavelength scale. However, the search for an efficient way to fabricate on demand artificial PBG structures in two dimensions and three dimensions, in a large scale, remains a challenge.

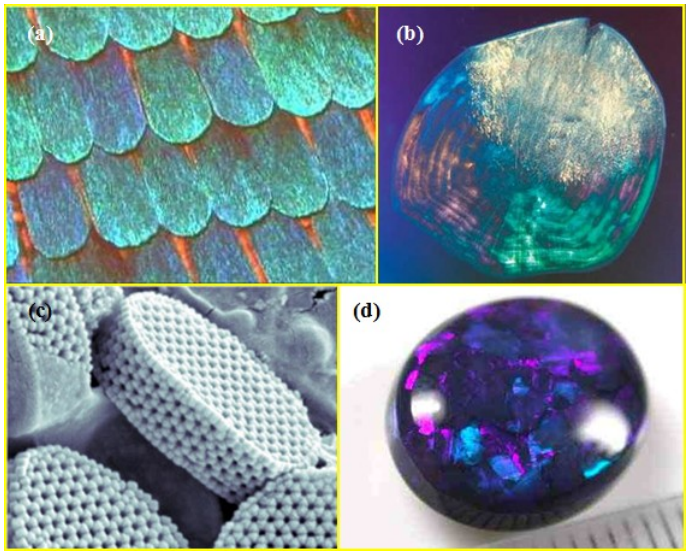

Figure 2.2 Natural photonic nanostructures: (a) scales on butterfly wings; (b) the fish fin gets metallic luster from multilayer of cytoplasm and crystals [19]; (c) double-layer calcite crystals shells on the alga Calyptrolithophora papillifera [20]; (d) an opal.

The period of the photonic crystals is usually engineered to be comparable with the wavelength of the incident light, which usually covers visible light, infrared and/or near infrared and microwave bands, whose wavelength typically ranging from hundreds of nanometers to several microns. By this design, the formed PBG could be located in these selected frequency ranges. While on the other side of the story, a long range of precisely ordered repetitive series have to be kept, making the structure periodic, thus, functional. The preparation on such a micro level hence is subject to fluctuations in the environment. Despite the difficulties, the persistent research and ingenious creativity have been rewarded with many promising techniques.

While dealing with a bulk material, a physical method is usually employed. For this reason, such kind of techniques is also called top-down approaches. Physical approaches have proven the efficiency for long wavelength, but not as ideal to be practiced in optical spectrum. Two major technique types are employed including electro-chemical etching and lithography techniques. The former method is mostly adopted in fabrication of two dimensional structures on porous materials. It is a relatively mature technique with the capability to fabricate nano-scale holes and pillars with high aspect ratios and highly ordered structures. However, this method suffers from several restrictions in processing three-dimensional structures, where it is usually not as simple and effective. The reports of such successful cases are scarce. Meanwhile, the candidates of porous materials with good quality are limited in silicon, Al_2O_3, and InP for quality consideration. The other large group of top-down techniques is the lithography. In terms of sources, the approaches use electron beam, ion beam, laser, x-ray, ultraviolet and so on. Based on different realization, there are generally three types: multi-photon/ink direct writing on photo-resist polymers, multi-beam interference, and holographic lithography. Of these methods, interference lithography receives more popularity for its ability to pattern large area at high speed. Though, it has the disadvantage of procedure complexity and lack of control over structure geometry [21]. Good news has been heard that the improvement in phase mask optics can avoid some parts of these challenges [22-25]. Generally speaking, the efficacy of top-down approaches has been proved in preparing long wavelength structures.

Chemistry bottom-up techniques offer an alternative perspective. Glancing angle deposition (GLAD) is such a technique in which nano-scale structures are deposited by particle beams. By controlling the angle of a beam, a variety of complex geometry can be obtained. Self-assembly of highly mono-disperse and spherical colloidal particles, on the other hand, shows a way of both ease of fabrication and low cost. In this process, colloidal particles automatically form a highly ordered structure, usually known as artificial opal. However, only the most stable structures can be developed into crystallization. One is the face-centered-cubic (FCC), and random hexagonal close packing (RHCP) the other [26]. There has been intense research interest aroused in FCC for the fact that it has the most spherical Brillouin zones, which could be a factor vital for the distinct effects of super lens and all angle negative refraction [27]. The colloidal crystals can be inverted using chemical vapor deposition (CVD) process, and the core could be eroded off and stuffed with different materials. Especially, by infiltrating liquid crystals or other electro-optical materials, the optical characters are tunable by an external electric field, enabling diversified properties. Self–assembly of non-spherical colloidal particles has also been proposed [28,29]. However the lack of long-range order suggests the difficulty to keep them strictly organized. Improvements have been heard that the fabrication process could be assisted with employing magnetic colonials along with an external magnetic field [26].

2.3 Theoretical Analyses

To comprehensively understand the property of such a diversified glossary of materials with finely arranged nano-scale geometry, the complexity is needless to mention. There have been a variety of analytical tools developed over the time, dedicated to the study of different aspects of the problem. The frequency difference time domain (FDTD) algorithm is a popular modeling technique to calculate the evolving and distribution of EM fields in a finite model. By obtaining the exact field distribution, spectra of transmission and scattering can also be acquired. The technique is intuitive in that it uses E and H fields directly, and records their changes in every time step. However, a mesh of decent resolution is required with step sizes generally smaller than both the characteristic wavelength and the size of the finest model feature. Therefore, for a large simulation domain, *esp*. three-dimensional systems, or with a high-frequency wavelength, the simulation is extremely consumptive in terms of computational resource and time. Distributed or parallel computation is usually required to facilitate the task.

The transfer matrix method (TMM) and the multiple scattering theory (MST) are usually employed to calculate scattering spectra, as well for reflection and transmission. Both methods use a similar process of passing solutions between neighbor layers or cell units. Finite models are used, in which the layers and cell units are supposed to be identical. In other words, the structure has perfect periodicity. The calculation is in frequency domain. Additionally, MST can be

adopted in the calculation of band structure for infinite ideal lattice. Especially, when decaying field is taken into account, it has a better performance than plane wave expansion method, which is usually used for such purpose.

Plane wave expansion (PWE) method is based on the concept of Bloch waves. The core idea is to calculate the dispersive relationship by solving an eigenvalue problem in a perfect and infinite large lattice. Therefore, band diagrams can be acquired by sampling the dispersive relationship within the first Brillion zone. Field components can be obtained in the same process. Thus field distribution for each mode could be plotted accordingly. The disadvantage lies in the requirement that the materials have positive and relatively constant dielectric permittivity. Metals and other highly dispersive materials cannot be efficiently solved for divergence problems. Analysis is mainly accomplished by PWE method in this thesis.

2.3.1 Plane Wave Expansion Method

The mathematical treating starts with the Maxwell equations.

$$\begin{cases} \nabla \cdot \boldsymbol{B}(\boldsymbol{x},t) = 0 \\ \nabla \cdot \boldsymbol{D}(\boldsymbol{x},t) = \eta(\boldsymbol{x},t) \\ \nabla \times \boldsymbol{H}(\boldsymbol{x},t) - \frac{\partial \boldsymbol{D}(\boldsymbol{x},t)}{\partial t} = \boldsymbol{J}(\boldsymbol{x},t) \\ \nabla \times \boldsymbol{E}(\boldsymbol{x},t) + \frac{\partial \boldsymbol{B}(\boldsymbol{x},t)}{\partial t} = 0 \end{cases} \tag{2.2}$$

where $\boldsymbol{E}$ is the electric field; $\boldsymbol{D}$ is the electric displacement field; $\boldsymbol{B}$ is the magnetic field; $\boldsymbol{H}$ is the magnetizing field. $\boldsymbol{x}$ and t indicate the location and time. Assumptions have been made that the media are sourceless, free of dispersion and

isotropic, thus charge density $\eta = 0$ and current density $\boldsymbol{J} = 0$. Considering the fact that the common materials used in PBG structures have very little magnetic effect, further restriction could be made as μ_r=1. So that the equations can be restated as

$$\boldsymbol{D}(\boldsymbol{x},t) = \varepsilon_0\varepsilon_r(\boldsymbol{x})\boldsymbol{E}(\boldsymbol{x},t); \quad \boldsymbol{B}(\boldsymbol{x},t) = \mu_0\mu_r\boldsymbol{H}(\boldsymbol{x},t) = \mu_0\boldsymbol{H}(\boldsymbol{x},t); \quad (2.3)$$

$$\begin{cases} \nabla \cdot \boldsymbol{H}(\boldsymbol{x},t) = 0 \\ \nabla \cdot \varepsilon_r(\boldsymbol{x})\boldsymbol{E}(\boldsymbol{x},t) = 0 \\ \nabla \times \boldsymbol{H}(\boldsymbol{x},t) - \varepsilon_0\varepsilon_r(\boldsymbol{x})\frac{\partial \boldsymbol{E}(\boldsymbol{x},t)}{\partial t} = 0 \\ \nabla \times \boldsymbol{E}(\boldsymbol{x},t) + \mu_0\frac{\partial \boldsymbol{H}(\boldsymbol{x},t)}{\partial t} = 0 \end{cases} \quad (2.4)$$

For time harmonic field, the factored expressions are:

$$\boldsymbol{E}(\boldsymbol{x},t) = \boldsymbol{E}(\boldsymbol{x})e^{-i\omega t}; \quad \boldsymbol{H}(\boldsymbol{x},t) = \boldsymbol{H}(\boldsymbol{x})e^{-i\omega t}; \quad (2.5)$$

By the substitution of $\frac{\partial^2}{\partial t^2} \to -\omega^2$, the decoupled equations can be expressed in the following form,

$$\begin{cases} \nabla \times [\varepsilon_r^{-1}(\boldsymbol{x})\nabla \times \boldsymbol{H}(\boldsymbol{x})] = \frac{\omega^2}{c^2}\boldsymbol{H}(\boldsymbol{x}) \\ \nabla \times \nabla \times \boldsymbol{E}(\boldsymbol{x}) = \varepsilon_r(\boldsymbol{x})\frac{\omega^2}{c^2}\boldsymbol{E}(\boldsymbol{x}) \end{cases} \quad (2.6)$$

The assumption we made in the beginning simplifies the expression for permittivity to a real quantity. However, it could be modified to accommodate the simulation with anisotropic media. At this stage, two equations are both eligible for further treatment. Either of them can be used to solve the problem, but the accuracy and complexity could vary in different cases. For example, for PhCs with air spheres embedded in dielectric backbone, E expansion is reported to have better convergence. While using $\boldsymbol{H}$ could yield better results for dielectric in air [30,31]. Without loss of generality, $\boldsymbol{H}$ field equation in (2.6) is used here. The periodic structure requires the solution satisfy the Bloch-Flouquet theorem,

$$\boldsymbol{H}(\boldsymbol{x}) \equiv \boldsymbol{H}_{\boldsymbol{k}}(\boldsymbol{x}) = \sum_{\boldsymbol{G}} \sum_{l=1}^{2} h_{\boldsymbol{G}}^{l} \boldsymbol{\sigma}_{\boldsymbol{G}}^{l} e^{i(\boldsymbol{k}+\boldsymbol{G})\cdot\boldsymbol{x}} \tag{2.7}$$

where $\boldsymbol{k}$ is a wave vector, l indicates two polarizations, h is the magnitude of magnetizing field, $\boldsymbol{\sigma}$ is the unit vector perpendicular to the wave vector, and $\boldsymbol{G}$ denotes the set of vectors of the reciprocal lattice. The Bloch modes can be considered as a series of plane waves modulated by the spatially repeated structure. Meanwhile, similar treatment should be applied to describe the lattice dielectric distribution. Expanding $\varepsilon_r^{-1}(\boldsymbol{x})$ in Fourier series of $\boldsymbol{G}$ gives,

$$\varepsilon_r^{-1}(\boldsymbol{x}) = \sum_{\boldsymbol{G}} \epsilon_{\boldsymbol{G}}^{-1} e^{i\boldsymbol{G}\cdot\boldsymbol{x}} \tag{2.8}$$

inserting (2.7) and (2.8) into (2.6) leads to an eigenvalue equation,

$$\sum_{\boldsymbol{G}'} \sum_{l'=1}^{2} |\boldsymbol{k}+\boldsymbol{G}||\boldsymbol{k}+\boldsymbol{G}'|(\boldsymbol{\sigma}_{\boldsymbol{G}}^{l} \cdot \epsilon_{\boldsymbol{G}-\boldsymbol{G}'}^{-1} \cdot \boldsymbol{\sigma}_{\boldsymbol{G}'}^{l'}) h_{\boldsymbol{G}'}^{l'} = \frac{\omega^2}{c^2} h_{\boldsymbol{G}}^{l} \tag{2.9}$$

where apostrophes are used to indicate another set of reciprocal vectors and polarizations, which are independent of $\boldsymbol{G}$ and l. The two different sets of vectors expand to an infinite matrix. The eigen-equation is then solved for specified $\boldsymbol{k}$ vectors. In practical calculation, the expression is truncated to a finite number of $\boldsymbol{G}$ and $\boldsymbol{G'}$ vectors, while ensuring enough accuracy is retained. The main procedure to solve (2.9) is to numerically evaluate the Fourier coefficients of (2.8). There are two ways to get the results as for isotropic materials [32]. One is the direct method in which the inverse dielectric coefficients in real space are calculated. In the other way, the coefficients are obtained in real space first, and their inverses are taken flowing. Owing to the linearity of both Fourier transformation and inversion operations, the two methods should give ultimately the same results. However, for truncated (2.9) in practical calculation, the second way excels in dramatic improved rates of convergence [33].

2.3.2 Analysis in hexagonal lattice

The following figure is an illustration of a two dimensional PhC, which is essentially a hexagonal lattice formed by circular air cells (n_{air} = 1) with radius of 0.4 μm embedded in silicon backbone (n_{Si} = 3.6). The crystal constant is a = 1 μm.

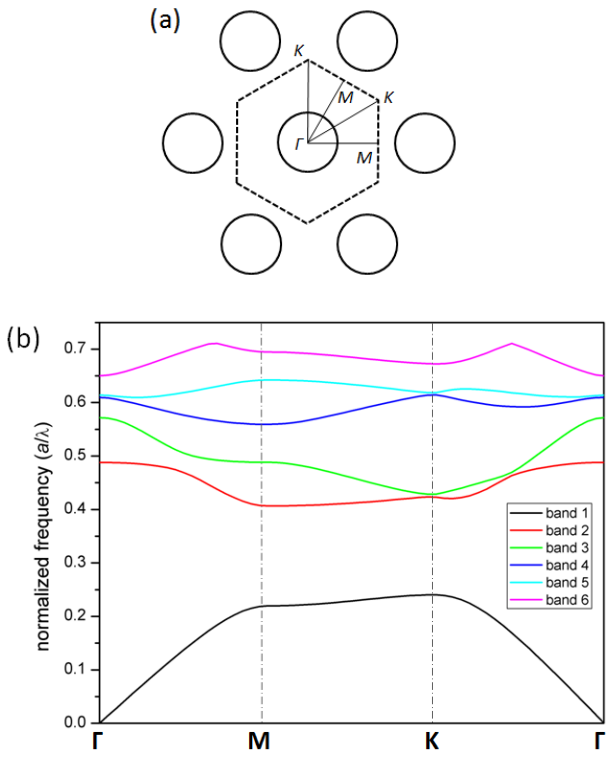

Figure 2.3 (a) A two-dimensional hexagonal PhC with air holes in silicon backbone; Dotted lines outlines the first Brillouin zone in the inverse space, with high symmetry points *Γ*, *K* and *M* labeled. It is also a hexagon, rotated by 30°. (b) The first six bands are shown in the diagram for TM mode. A complete band gap of ($\Delta\omega/\omega_{center}$) around 52.3% is identified.

The reciprocal lattice is also hexagonal. *M* and *K* stands for the high symmetry points on the boundary of the first Brillouin zone (FBZ), while *Γ* is origin. Implementation of the PWE method is carried out for transverse magnetic (TM) mode, i.e. the $\boldsymbol{H}$ field lies perpendicularly to the structure plane. For transverse electric (TE) mode, that would be the $\boldsymbol{E}$ field. The band diagram is calculated by sampling the $\boldsymbol{k}$ points in the inverse space along the path *Γ*-*M*-*K*-*Γ*, which is converted to the horizontal axis in Fig. 2.3(b). The diagram is able to show all the maxima and minima of the frequency in each band within FBZ, and as a result of the periodicity of the reciprocal lattice, the results account for the entire structure.

Band diagram is a quick and direct way to identify the location and size of the band gaps. However, in some situations information drawn from a simple path is insufficient to characterize the distribution of the dispersion relation in the whole reciprocal space. In this case, a full sampling of the area to include the FBZ, or equivalently a primitive cell in the reciprocal lattice, is necessary. The method starts with meshing of the area with fine grids. The PWE calculation is carried out on each grid point. The higher resolution the mesh is deployed, the more detailed inform could be revealed. The $\boldsymbol{k}$ points with similar frequency can be subsequently linked to form contour lines, which are termed equifrequency contours (EFCs).

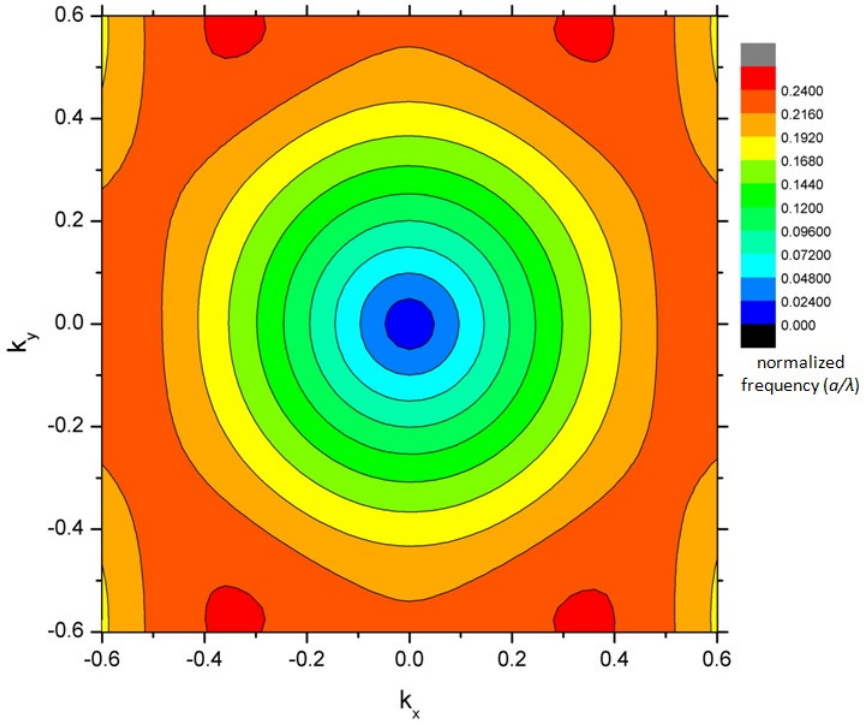

Figure 2.4 EFCs of the 1st band of TM mode for the structure in Fig. 2.3. The frequency range is coded in colors, indicated by the color bar on the right side.

The EFCs patterns bear the same symmetry elements with the lattice. Further, provided the expression of group velocity in (2.1), the direction of gradient is always perpendicular to the EFCs. The fact shows the special importance of EFCs in analyzing the light propagation.

2.3.3 Density of states

One of the most important characters of the PBG structures is its ability to rearrange the density of states (DOS), to which the different quantum features are closely related. The density of states describes the number of wave vectors, i.e. optical modes, which can be allowed to exist in a system per interval frequency at

each frequency level. Low DOS in photonic band gap leads to bound photon-atom states, suppressed photon emission, and strong localization [33-35]. Further, the inhibited spontaneous emission rate can reduce the lasing threshold of a laser or the decay rate of a dipole emitter [36]. Recent investigation for accurate modeling and deep micro-level processing puts a higher demand on acquiring the local density of state (LDOS). It should be mentioned that, by introducing defects into the elsewhere perfect lattice, defect modes can be created within the band gaps. It is of particular meaning to model and control the LDOS on the defect sites.

The approaches to theoretically obtain the DOS and LDOS are diversified, including Green's tensor, MSC, TMM [37-40]. Based on the previous PWE analysis, DOS and LDOS can be readily drawn from the results. The definitions are expressed as,

$$\rho(\omega) = \sum_n \delta(\omega - \omega_n) = \sum_n \int \delta(\omega - \omega_n(\boldsymbol{k}))d\boldsymbol{k}, \text{ for DOS} \qquad (2.10)$$

$$\rho(\omega, \boldsymbol{x}) = \sum_n \left|\boldsymbol{E}_{n,\boldsymbol{k}}(\boldsymbol{x})\right|^2 \delta(\omega - \omega_n)$$

$$= \sum_n \int \left|\boldsymbol{E}_{n,\boldsymbol{k}}(\boldsymbol{x})\right|^2 \delta(\omega - \omega_n(\boldsymbol{k}))d\boldsymbol{k}\text{ , for LDOS} \qquad (2.11)$$

where n is used to denote the frequency levels. The density of states is represented as ρ of The integration is usually made in the FBZ or the primitive cell in the inverse space. In previous procedures, the FBZ has been mapped with a mesh, and the eigen-frequency for each grid in the FBZ has been obtained. By counting $\boldsymbol{k}$ points within frequency slots, the calculation of DOS and LDOS can be done in a histogram way (Fig. 2.5) [41,42]. The method is therefore straightforward.

Attention should be paid to the restriction on frequency resolution $\Delta\omega$ relating the mesh fineness [42,43],

$$\Delta\omega \approx \Delta k|\nabla_{\boldsymbol{k}}\omega| \tag{2.12}$$

The criterion predicts that over narrowed histogram bins can bring unphysical and fake spikes in DOS and LDOS charts. It is noteworthy that for zero DOS, LDOS would be zero everywhere. While on the other way, zero LDOS does not necessarily imply zero DOS, for there are nodes of field distribution for every mode. DOS of the hexagonal PhC described in Fig. 2.3 is obtained for TM modes only. The results are presented as a histogram in Fig. 2.5. A band gap can be found represented by a blank area between 0.25 and 0.39.

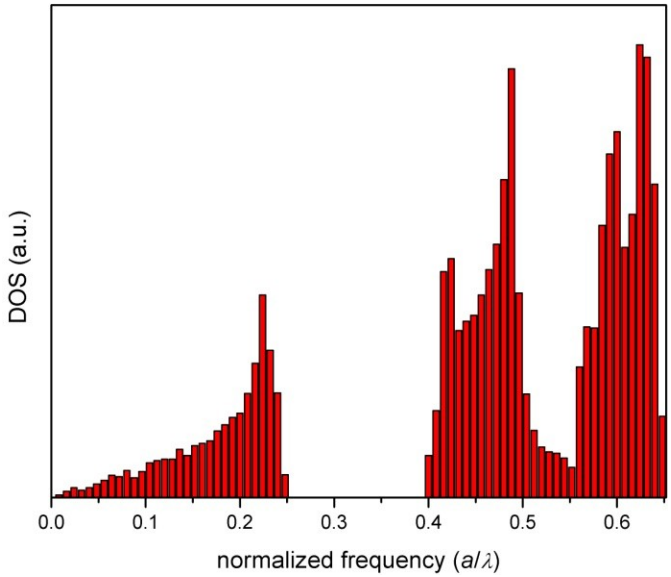

Figure 2.5 DOS in the structure demonstrated in Fig. 2.3. The result is presented as a histogram.

References

[1] M. Inoue, K. Arai, T. Fujii, and M. Abe, "Magneto-optical properties of one-dimensional photonic crystals composed of magnetic and dielectric layers," *Journal of Applied Physics*, vol. 83, 1998, p. 6768.

[2] J.D. Joannopoulos, P.R. Villeneuve, and S. Fan, "Photonic crystals: putting a new twist on light," *Nature*, vol. 386, 1997, pp. 143-149.

[3] J.S. Foresi and L.C. Kimerling, "letters to nature microcavities in optical waveguides," *Nature*, 1997, pp. 143-145.

[4] S. Fan, S.G. Johnson, J.D. Joannopoulos, C. Manolatou, and H.a. Haus, "Waveguide branches in photonic crystals," *Journal of the Optical Society of America B*, vol. 18, 2001, p. 162.

[5] Y.a. Vlasov, X.Z. Bo, J.C. Sturm, and D.J. Norris, "On-chip natural assembly of silicon photonic bandgap crystals.," *Nature*, vol. 414, 2001, pp. 289-93.

[6] M. Qi, E. Lidorikis, P.T. Rakich, S.G. Johnson, J.D. Joannopoulos, E.P. Ippen, and H.I. Smith, "A three-dimensional optical photonic crystal with designed point defects.," *Nature*, vol. 429, 2004, pp. 538-42.

[7] M. Notomi, A. Shinya, S. Mitsugi, G. Kira, E. Kuramochi, and T. Tanabe, "Optical bistable switching action of Si high-Q photonic-crystal nanocavities.," *Optics express*, vol. 13, 2005, pp. 2678-87.

[8] Y. Zhang, M.W. McCutcheon, I.B. Burgess, and M. Loncar, "Ultra-high-Q TE/TM dual-polarized photonic crystal nanocavities.," *Optics letters*, vol. 34, 2009, pp. 2694-6.

[9] M.W. McCutcheon, D.E. Chang, Y. Zhang, M.D. Lukin, and M. Loncar, "Broad-band spectral control of single photon sources using a nonlinear photonic crystal cavity," *Optics Express*, vol. 17, 2009, p. 9.

[10] M.W. Mccutcheon, D.E. Chang, Y. Zhang, and M.D. Lukin, "Broad-band spectral control of single photon sources using a nonlinear photonic crystal cavity," *Quantum*, 2009, pp. 1-9.

[11] J. Bravo-Abad, A. Rodriguez, P. Bermel, S.G. Johnson, J.D. Joannopoulos, and M. Soljacic, "Enhanced nonlinear optics in photonic-crystal microcavities.," *Optics express*, vol. 15, 2007, pp. 16161-76.

[12] M. McCutcheon, J. Young, G. Rieger, D. Dalacu, S. Frédérick, P. Poole, and R. Williams, "Experimental demonstration of second-order processes in photonic crystal microcavities at submilliwatt excitation powers," *Physical Review B*, vol. 76, 2007, pp. 1-6.

[13] F. Raineri, C. Cojocaru, P. Monnier, a. Levenson, R. Raj, C. Seassal, X. Letartre, and P. Viktorovitch, "Ultrafast dynamics of the third-order nonlinear response in a two-dimensional InP-based photonic crystal," *Applied Physics Letters*, vol. 85, 2004, p. 1880.

[14] M. Liscidini and L.C. Andreani, "Highly efficient second-harmonic generation in doubly resonant planar microcavities," *Applied Physics Letters*, vol. 85, 2004, p. 1883.

[15] M. Soljacić and J.D. Joannopoulos, "Enhancement of nonlinear effects using photonic crystals.," *Nature materials*, vol. 3, 2004, pp. 211-9.

[16] S. John, "Light control at will," *Nature*, vol. 460, 2009, pp. 2009-2009.

[17] T. Baba, "Slow light in photonic crystals," *Nature Photonics*, vol. 2, 2008, p. 465–473.

[18] T. Baba and D. Mori, "Slow light engineering in photonic crystals," *Journal of Physics D: Applied Physics*, vol. 40, 2007, pp. 2659-2665.

[19] A. Levy-Lior, B. Pokroy, B. Levavi-Sivan, L. Leiserowitz, S. Weiner, and L. Addadi, "Biogenic Guanine Crystals from the Skin of Fish May Be Designed to Enhance Light Reflectance," *Crystal Growth & Design*, vol. 8, 2008, pp. 507-511.

[20] R. Quintero-Torres, J. Aragón, M. Torres, M. Estrada, and L. Cros, "Strong far-field coherent scattering of ultraviolet radiation by holococcolithophores," *Physical Review E*, vol. 74, 2006, pp. 2-5.

[21] D. Shir, E.C. Nelson, Y.C. Chen, a. Brzezinski, H. Liao, P.V. Braun, P. Wiltzius, K.H. Bogart, and J.a. Rogers, "Three dimensional silicon

photonic crystals fabricated by two photon phase mask lithography," *Applied Physics Letters*, vol. 94, 2009, p. 011101.

[22] Y. Nam, S. Jeon, D. Shir, A. Hamza, and J. Rogers, "Thick, three-dimensional nanoporous density-graded materials formed by optical exposures of photopolymers with controlled levels of absorption," *Applied optics*, vol. 46, 2007, p. 6350–6354.

[23] D.J. Shir, S. Jeon, H. Liao, M. Highland, D.G. Cahill, M.F. Su, I.F. El-Kady, C.G. Christodoulou, G.R. Bogart, A.V. Hamza, and J.a. Rogers, "Three-dimensional nanofabrication with elastomeric phase masks.," *The journal of physical chemistry. B*, vol. 111, 2007, pp. 12945-58.

[24] S. Lee, H.S. Park, G. Yi, J.H. Moon, and S. Yang, "Holographic fabrication of microstructures with internal nanopatterns using microprism arrays.," *Angewandte Chemie (International ed. in English)*, vol. 48, 2009, pp. 7000-5.

[25] M. Maldovan, C. Ullal, J. Jang, and E. Thomas, "Sub-Micrometer Scale Periodic Porous Cellular Structures: Microframes Prepared by Holographic Interference Lithography," *Advanced Materials*, vol. 19, 2007, pp. 3809-3813.

[26] T. Ding, K. Song, K. Clays, and C. Tung, "Fabrication of 3D Photonic Crystals of Ellipsoids: Convective Self-Assembly in Magnetic Field," *Advanced Materials*, vol. 21, 2009, pp. 1936-1940.

[27] C. Luo, S.G. Johnson, and J.D. Joannopoulos, "All-angle negative refraction in a three-dimensionally periodic photonic crystal," *Applied Physics Letters*, vol. 81, 2002, p. 2352.

[28] Q. Yan, Z. Zhou, and X. Zhao, "Inward-growing self-assembly of colloidal crystal films on horizontal substrates," *Langmuir*, 2005.

[29] I. Hosein and C. Liddell, "Convectively assembled nonspherical mushroom cap-based colloidal crystals," *Langmuir*, 2007.

[30] A.J. Danner, "An introduction to the plane wave expansion method for calculating photonic crystal band diagrams," 2005, pp. 1-18.

[31] H. Sözüer, J. Haus, and R. Inguva, "Photonic bands: Convergence problems with the plane-wave method," *Physical Review B*, vol. 45, 1992, pp. 13962-13972.

[32] K. Busch and S. John, "Photonic band gap formation in certain self-organizing systems," *Physical Review E*, vol. 58, 1998, pp. 3896-3908.

[33] K. Busch and S. John, "Liquid-Crystal Photonic-Band-Gap Materials: The Tunable Electromagnetic Vacuum," *Physical Review Letters*, vol. 83, 1999, pp. 967-970.

[34] S. John, "Localization of Light," *Physics Today*, vol. 44, 1991, p. 32.

[35] S. John, "Strong localization of photons in certain disordered dielectric superlattices," *Physical Review Letters*, vol. 58, 1987, p. 2486–2489.

[36] A.H. Baradaran Ghasemi, S. Khorasani, H. Latifi, and A.H. Atabaki, "Calculation of density of states in a 2D photonic crystal with separable profile of permittivity," *Proceedings of SPIE*, vol. 6901, 2008, pp. 69010R-69010R-11.

[37] D.P. Fussell, R.C. McPhedran, and C. Martijn de Sterke, "Three-dimensional Green's tensor, local density of states, and spontaneous emission in finite two-dimensional photonic crystals composed of cylinders," *Physical Review E*, vol. 70, 2004, pp. 1-19.

[38] A. Moroz, "Minima and maxima of the local density of states for one-dimensional periodic systems," *Europhysics Letters (EPL)*, vol. 46, 1999, pp. 419-424.

[39] M. Wubs and a. Lagendijk, "Local optical density of states in finite crystals of plane scatterers," *Physical Review E*, vol. 65, 2002, pp. 1-12.

[40] Y. Xu, J.S. Vučković, R.K. Lee, O.J. Painter, A. Scherer, and A. Yariv, "Finite-difference time-domain calculation of spontaneous emission lifetime in a microcavity," *Journal of the Optical Society of America B*, vol. 16, Mar. 1999, p. 465.

[41] H. Monkhorst and J. Pack, "Special points for Brillouin-zone integrations," *Physical Review B*, vol. 13, 1976, pp. 5188-5192.

[42] I.S. Nikolaev, W.L. Vos, and A.F. Koenderink, "Accurate Calculation of the local density of optical strates in inverse-opal photonic crystals," *Journal of the Optical Society of America B*, vol. 26, 2009, p. 987.

[43] G. Gilat, "Analysis of methods for calculating spectral properties in solids," *Journal of Computational Physics*, vol. 10, 1972, pp. 432-465.

CHAPTER 3

Tunability in Two-Dimensional PhCs

Two-dimensional PBG structures have attracted special attention in that, comparing with the three-dimensional structures, the ease of fabrication significantly lowers the threshold for applications. There have been mature techniques available, both fast and cost effective, in association with fabrication and processing procedures nowadays. Delicate structure modification, e.g. line and point defects, could be precisely introduced and controlled. On the other hand, a large array of potential applications have been envisioned and realized, including PhCs lasers, fibers, waveguides, multipelxers, and demultiplexers. As well, the attached various physical phenomena have been intensively investigated, such as enhancement of stimulated emission, high harmonic generation, and enhancement of quadratic phase squeezing [1]. Underlying these topics, the ability to manipulate the light propagation and control the beam shape is of particular interest.

Attracted by the versatility of PhCs, researchers move on to the pursuit of active modulation of the devices, to fulfill different application requirements and optimize specific functionalities. Various schemes have been proposed to realize the tuning of the characters. In this chapter, a tuning method is proposed in two-dimensional PBG structures. The effects on light propagation and density of states are discussed. The work is based on the collaboration with Dr. Hao Wang. She contributed great efforts in the creative design of the scheme.

3.1 Introduction

3.1.1 Refraction in PhCs

With the distinctive dispersion relation arising from anisotropy and periodicity, PhCs modify the propagation of light diversely with respect to the wave vector and frequency, leading to extraordinary refraction characters. The super collimation or self-collimation could be such a case. In this situation, a light beam will not spread over the propagation. Unlike spatial soliton, the phenomenon is a linear effect independent of light intensity. By proper design, PhCs can support collimation for incidence in certain directions. Application is expected in the area of integrated optical circuits, helping with optical routing and logic [2]. Related work has been explosive since the earliest demonstration by H. Kosaka and their colleagues at NEC in Japan in 1999 [3]. The efforts have been mostly focused on the target wavelength for telecommunications (1260 – 1675 nm).

To theoretically identify the capability of super collimation in PhCs, the dispersion relation is analyzed. Given the introduction of EFCs in the previous chapter, the difference between homogeneous and inhomogeneous media could be pictorialized as that between circular (isotropic) EFCs and odd (anisotropic) ones. Since the group velocity is always perpendicular to the contour lines at the tips of $\boldsymbol{k}$ vectors, the shape of contour lines determines the passage of the light regarding its incident angle and frequency, therefore the shape of a not strictly straight light beam could be reshaped. For example, the wave vector of real light beam always consists of a small range. In the case of convex EFCs, with a small initial angle,

the spread will grow over distance. However, flat segments on EFCs can be found in PhCs, meaning the small group of different wave vectors will have a parallel output, in other words, the beam is collimated. The idea is shown in the Fig. 3.1. The central red dotted circle indicates the EFC of normalized frequency 0.182 in the air. Contours around the corners belong to a PhC with square lattice. The 0.182 contour has flat segments, contributing to the collimation of the blue light beam.

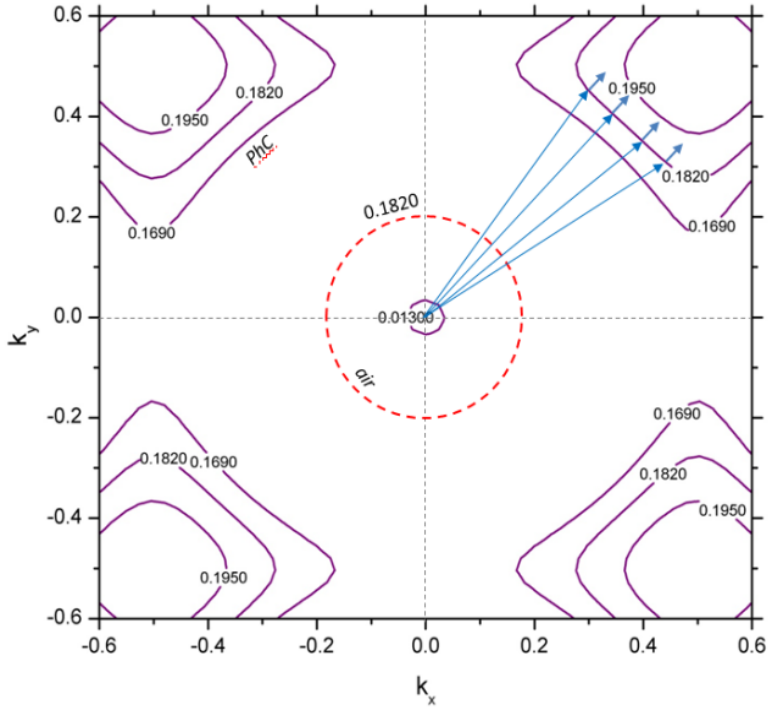

Figure 3.1 The purple curves are EFCs of a silicon-backbone-air-hole PhC with square lattice. The filling ratio is r/a = 0.4. The 0.182 EFC in air is given in red dotted circle. The blue light cone is collimated in the PhC.

In 1960s, Veselago *et al*. analyzed a structure with negative refractive index. In such system, the directions of electric field ***E***, magnetic field ***H*** and the wave

vector $\boldsymbol{k}$ form a "left handed" relation, for which Veselago coined the term left handed material (LHM). Metamaterials have been proposed in the past few years, shedding light on the realization of such strange materials. A metamaterial is usually composed of periodic sub-wavelength metal units. In particular spectrum regime, the metal structures couple with the incident EM waves, giving rise to both negative effective dielectric permittivity and magnetic permeability, hence the negative refractive index. The unit cells are usually made of one split ring resonator (SRR) combined with a conductive rod. Negative refraction has also been discovered in PhCs [4-7]. In contrast with LHM, the effect produced by this diffraction does not come from a left-handed relation. Use of highly conductive materials is not necessary. Therefore this scheme avoids the annoying issues of absorption loss and narrow band width due to the requirement of resonance [8-13]. With the aid of EFCs, negative refraction in PhCs could be easily illustrated in Fig. 3.2. An incident beam of normalized frequency 0.2765 enters the PhC from air on the left side, with its wave vector $\boldsymbol{k}_{air}$ pointing up-rightly. The conservation laws on the interface demands the refracted beam have the same value for the wave vector's parallel component. The frequency of EFCs in particular bands, here the 2nd band, rises inwardly, allowing the group velocity pointing to the opposite side of the normal line.

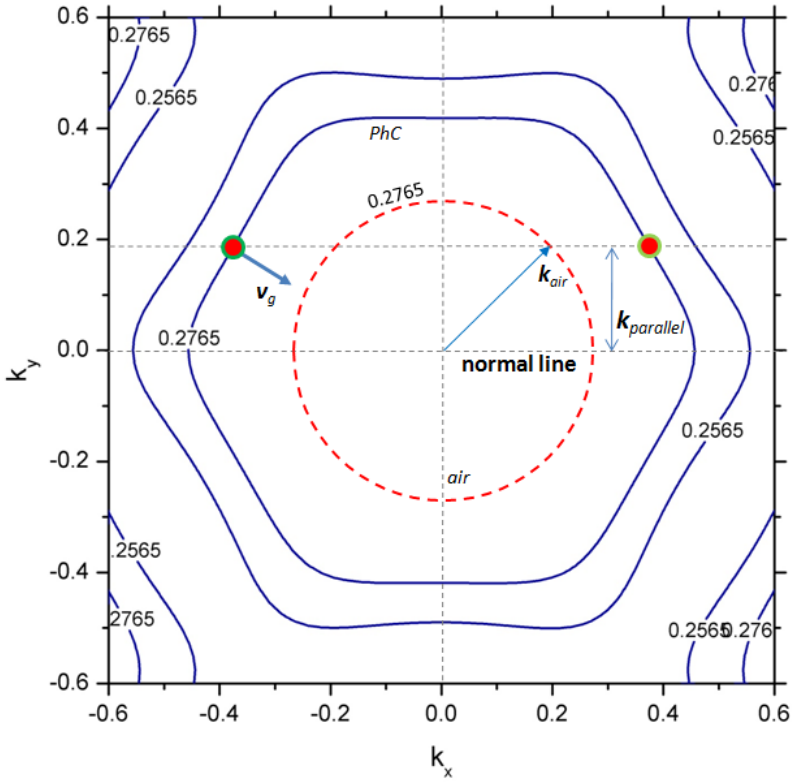

Figure 3.2 Beam incident from air enters the hexagonal PhC on the left, at an angle of 45°. The 0.2765 EFC of air is given in red dotted circle, combined with the 2nd band EFCs of the PhC. The boundary condition requires the component of $\boldsymbol{k}$ which is parallel to the surface should conserve on both sides, which leads to two points (red dots) on the EFC. Given group velocity is perpendicularly to the 0.2765 EFC, and points both towards higher frequency and into the PhC side, the left dot is identified as a practical solution to support light propagation. As a result of the refraction $\boldsymbol{v}_g$ is deflected downwards, pointing to the opposite direction with regard to the horizontal normal line.

The concept of negative refraction pushed the frontier of optics greatly forward. Potential applications have been envisioned. Among them, the idea of perfect lens (super lens) mentioned by Pendry is extraordinary [10]. A properly configured PhC slab could reverse the otherwise dissipating evanescent waves back to the

image, contributing extra fine structure information missing from traditional optical imaging systems, and thereby breaking the restriction that details could not be obtained in imaging on a sub-wavelength level. The effect has been intensively investigated. Up to now, both theoretical and experimental results have shown the trace of this behavior [9,14].

3.1.2 Achieving tunability

To take advantage of the versatility of the PBG functionalities, it is desirable to implement control and tuning on either structure or material property. In the former aspect, efforts have been focused on the changing of the geometric property. In some cases, PhCs are constructed in a highly anisotropic way, such as using oblate colloidal building blocks or by "post crystallization treatments" [11-13]. There are also more flexible ways allowing actively modulating the PhCs, through mechanic pressure, thermal effects and electro-optic effects [14-21]. The liquid crystals (LCs) have been chosen as a popular infill candidate owing to the fact that their properties can be changed efficiently by applying thermal, optical and electrical approaches [18-25].

Molecules of nematic LC lie randomly orientated when no external field is applied. The dielectric permittivity can be viewed as an average and thus isotropic index n_0. The idea is usually pictured as a sphere in the refractive index space. As the external field rises, molecules gradually line up along this direction, hence the index sphere will be prolonged or compressed to be a spheroid. Saturation will be reached when all the particles are strictly aligned, with external field E_{sat}. The

idea is shown in Fig. 3.3. A positive axial LC is demonstrated, in which the extraordinary refractive index n_e grows larger than the ordinary index n_o, i.e. $\Delta n = n_e - n_o > 0$.

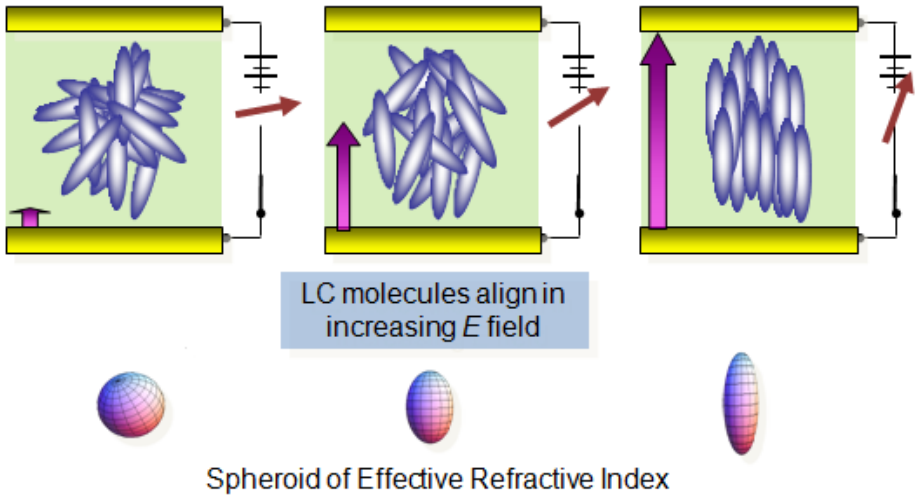

Figure 3.3 Anisotropy grows in the spheroid of LC dielectric permittivity as the ***E*** field rises. A prolate spheroid is given for the positive axial (Än > 0) model.

Modification therefore is needed to take the anisotropic permittivity into the mathematical model. In the governing equation (2.6), the scalar function $\mathring{a}_r(\boldsymbol{x})$ is substituted with tensorial form [34],

$$\boldsymbol{\varepsilon}_r(\boldsymbol{x}) = \varepsilon_{bg} + \left(\boldsymbol{\varepsilon}_{LC} - \varepsilon_{bg}\right)\sum_{\boldsymbol{R}} S(\boldsymbol{x} - \boldsymbol{R}), \qquad (3.1)$$

where $\boldsymbol{\varepsilon}_r(\boldsymbol{x})$ and $\boldsymbol{\varepsilon}_{LC}$ are third-order dielectric tensors. The function $S(\boldsymbol{x})$ equals 1 for those $\boldsymbol{x}$ falling inside the LC cells. $\boldsymbol{R}$ is the set of vectors in the real lattice. To avoid the mess of treating the off-diagonal terms, a rotation operation can be conveniently applied on the lattice, to allow the index spheroid of anisotropic LC sitting uprightly in the calculation coordinates.

$$\boldsymbol{\varepsilon}_{LC} = \begin{pmatrix} \varepsilon_{11} & \varepsilon_{12} & \varepsilon_{13} \\ \varepsilon_{21} & \varepsilon_{22} & \varepsilon_{23} \\ \varepsilon_{31} & \varepsilon_{32} & \varepsilon_{33} \end{pmatrix} = \boldsymbol{Q}^{\boldsymbol{T}} \begin{pmatrix} \varepsilon_x & 0 & 0 \\ 0 & \varepsilon_y & 0 \\ 0 & 0 & \varepsilon_z \end{pmatrix} \boldsymbol{Q} \quad , \qquad (3.2)$$

$\boldsymbol{Q}^{\boldsymbol{T}}$ is the inverse and transposed matrix of $\boldsymbol{Q}$. The dielectric function can then be expanded in Fourier series of the "rotated" reciprocal vectors $\boldsymbol{G}_{new} = \boldsymbol{QG}$. The equations (2.6) can thereby separated into three independent equations.

3.2 Two-dimensional tunable PhC with nematic LC infill

In this part, a 2D hexagonal PhC slab composed of holes array is proposed. The objective is to actively tune the refraction character by an external electric field, realizing positive/negative refraction and total reflection at one frequency. To avoid high-order scattering related to multi-reciprocal vector processes, lower, hence smoother bands are preferred. Thus the primary option is to locate one particular frequency that transits among the first band, the second band and the band gap in between, with electric tuning applied. Nematic LC is filled in the orifices, with the refractive index being n_0 = 1.8 for the untuned situation, and in saturation n_o = 2.2, n_e = 1.6 [31].This is a material with negative dielectric anisotropy (Δå < 0). High-index germanium (n_{Ge} = 4.3) backbone is deployed. The lattice constant a is set at one micron. This structure is a modified version of the air-hole-dielectric-backbone PhC. Previous study [32] indicates that hexagonal lattice could give rise to larger band gaps. A complete band gap for both TE and TM modes is also desirable (Fig. 3.4). In regard of this, the hexagonal lattice is preferred over the square ones.

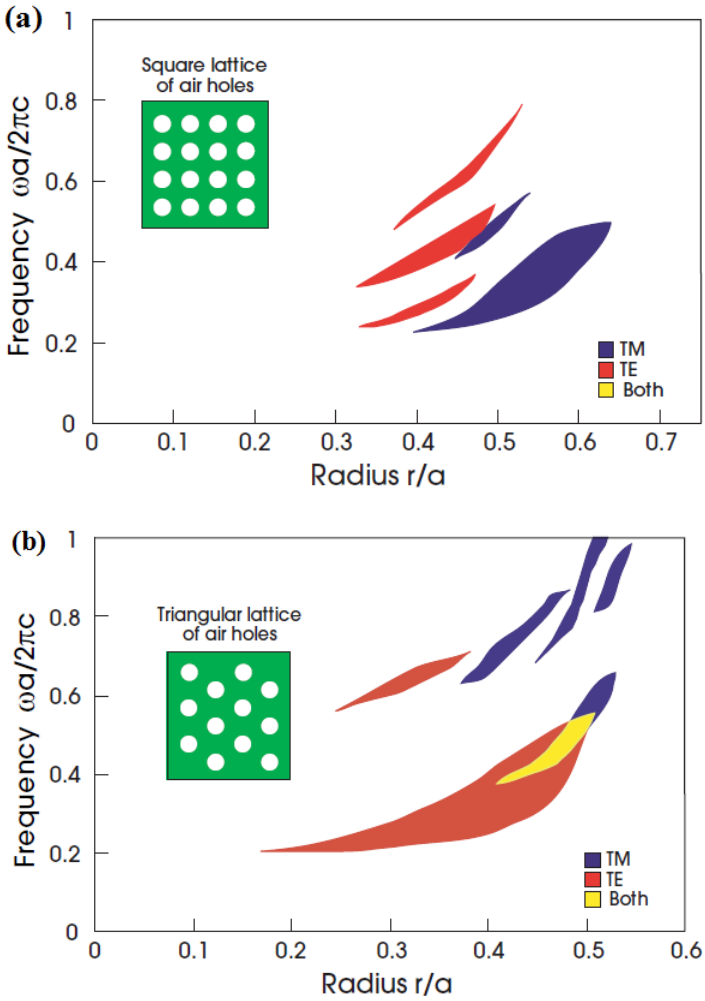

Figure 3.4 Band gap maps for air holes in (a) square and (b) hexagonal (triangular) lattices, with a backbone (green) index 3.38. The definition of TE and TM is contrary to those in this thesis) [32].

The setup is demonstrated as following (Fig. 3.5). The two-dimensional PBG slab is modulated by a vertical (z direction) external electric field, controlled by a voltage source. As the field intensity increases, the in-plane TE wave will experience a lower refractive index n_e, while TM polarization has a rising n_o. Calculation for both polarizations is of no difference from that for wave travelling

in a PhC composed of isotropic media. What only matters is the value of the scalar refractive index. Thus the complexity of the problem is largely reduced.

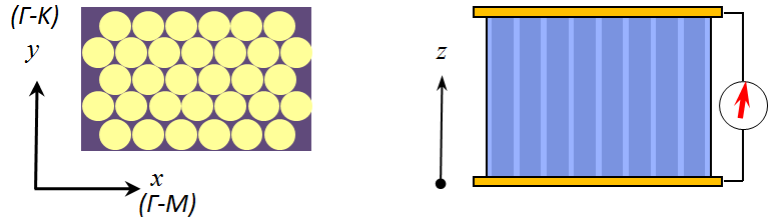

Figure 3.5 On the left is the top view of a two-dimensional hexagonal PhC. Scheme for vertical tuning is shown on the right side. The electric field is applied along *z* direction.

Fig 3.4(b) also indicates the higher probability to locate a band gap in high filling ratio area. For easy fabrication, slabs with a *r*/*a* around 0.4 are desirable [33]. Given these thoughts, the TM band structures for three ratio sets of 0.4, 0.44, and 0.48 are analyzed, matched with LC index pair (n_o, n_e) being (1.8, 1.8), as not tuned, and (2.2, 1.6), as saturation reached. The results are shown in fig 3.6. The TE modes do not have a band gap, despite the altering of the filling ratio. The tuning of LC index has little effect on them, as well. As for TM modes, there lies a gap for 0.40 and 0.44 *r*/*a*, where no frequency could be allowed for transition among the three states. As the ratio goes up, the gap closes. On the other hand, the larger volume the LC holes take up, the larger range of tuning can be achieved, and thus the wider can the red/green band curves separate from the black ones in the band diagram. In the band diagrams for 0.48 *r*/*a*, intersection of the first band, the second band and the gap between them can be found around the normalized frequency 0.25.

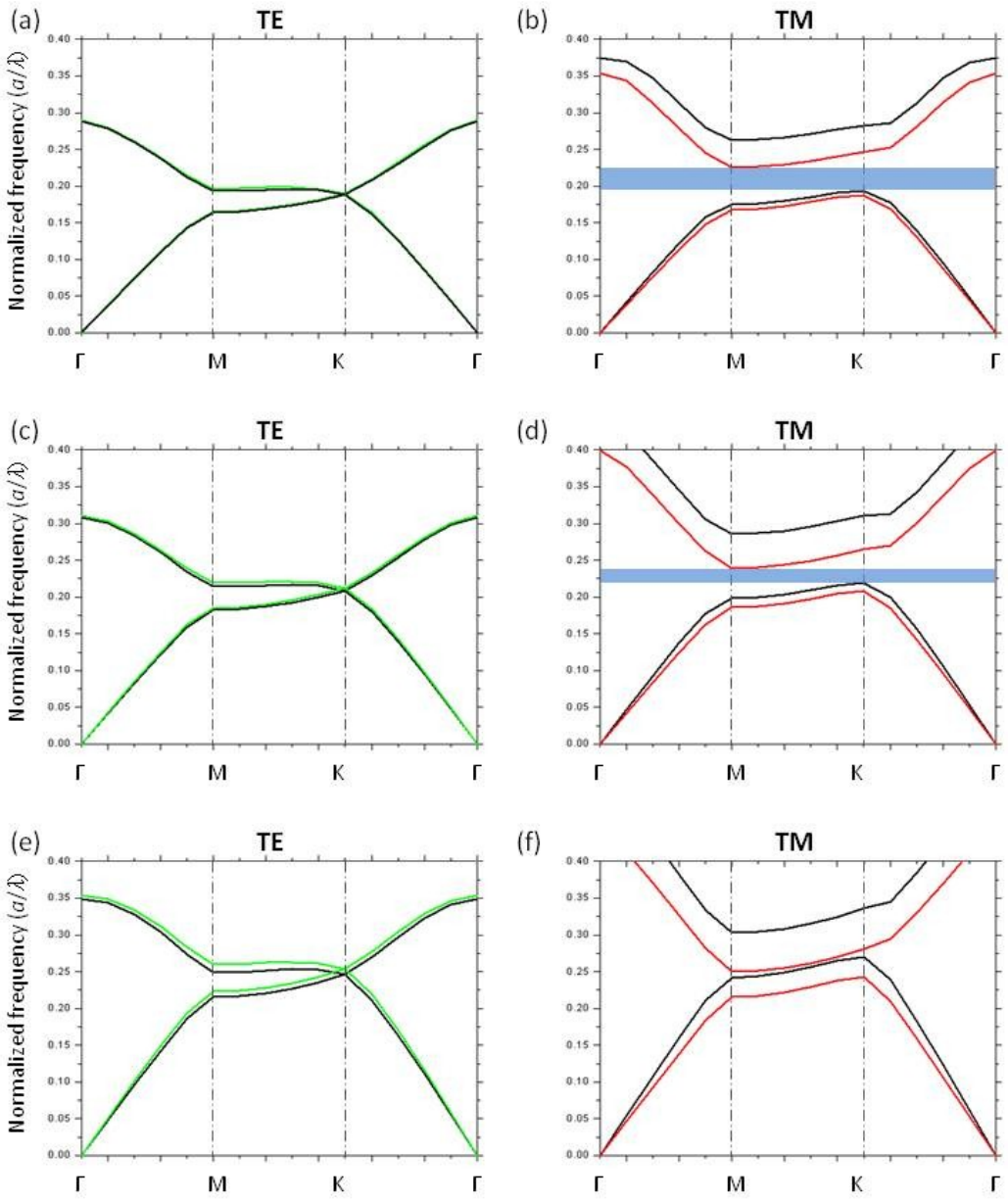

Figure 3.6 The first two photonic bands of Ge-based 2D PhCs with *r*/*a* set at (a) and (b) 0.40, (c) and (d) 0.44, (e) and (f) 0.48, respectively. Green, black, and red represent the refractive indices: 1.6, 1.8 and 2.2, respectively; TE mode on the left, TM right.

A close examination of the EFCs in Fig. 3.7 illustrates the positive refraction in the first band of TM mode with the LC index of 1.8, and negative refraction in the

second band of TE mode with the index of 1.8. The incident angle *è* is set at 14° with respect to the *Γ*-*M* (*x* axis) direction. A buffer layer of Ge is adopted to scale up the incident wave vector. By this setup, it can reach the optimized EFC segment featuring negative refraction. The parallel component of the wave vector is designed as, $k_{\parallel} = k_y = k_0 \times n_{Ge} \sin\theta = 0.26$.

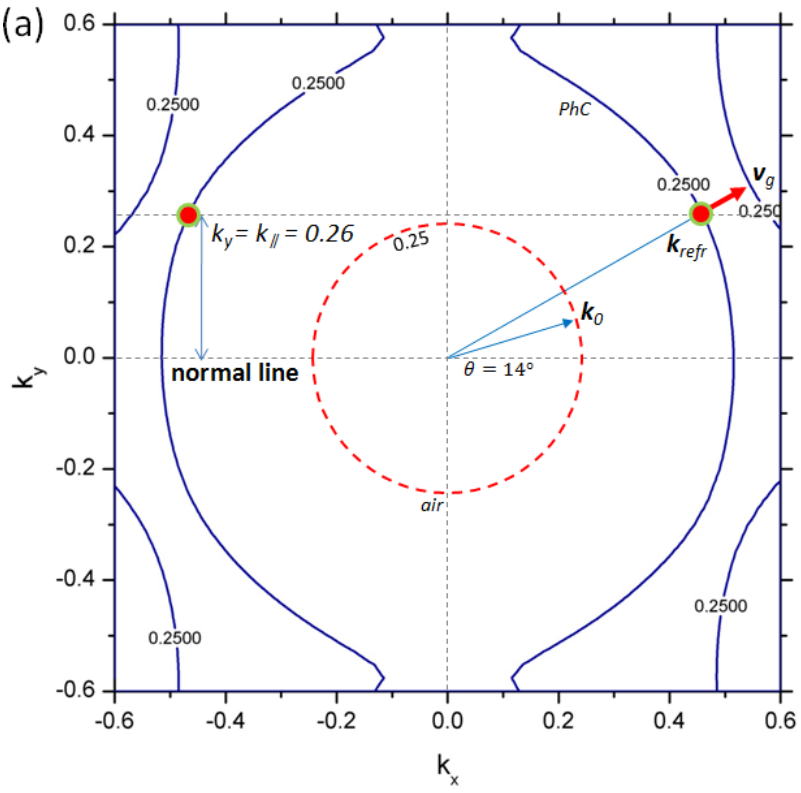

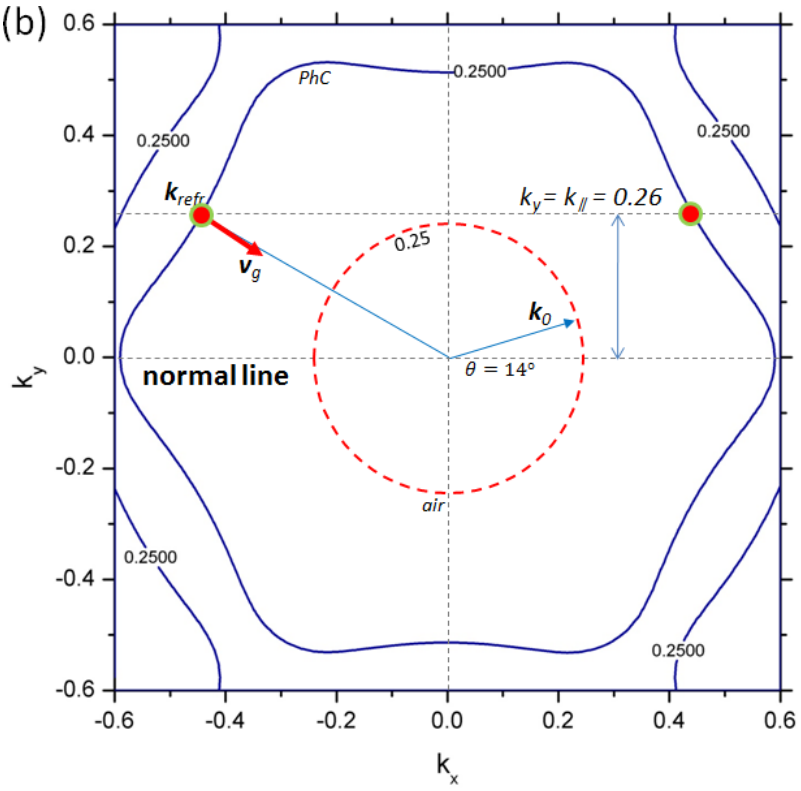

Figure 3.7 EFCs of (a) the first band of TM mode; positive refraction (b) the second band of TE mode; negative refraction. LC index is 1.8, with filling ratio 0.48. Red arrow $\boldsymbol{v}_g$ indicates the refraction directions. $\boldsymbol{k}_0$ is the original incident wave vector, along which the incident light enters from the air. $\boldsymbol{k}_{refr}$ is the wave vector of the refraction. The incident angle between $\boldsymbol{k}_0$ and the normal line is set to be θ = 14°. The identification of refraction follows the same procedure described in Fig. 3.2. Firstly, by forcing the parallel component of the wave vector to conserve in both media, potential solutions (red dots) are located on the 0.25 EFC. Considering the group velocity should (1) be perpendicular to the EFC and (2) point both towards higher frequency and (3) into the PhC side, the refraction is thereby determined.

FDTD simulation is employed to verify the light propagation in the PhC predicted by the EFSs analysis. The model is set up as shown in Fig. 3.8. A twelve-layer

hexagonal PhC slab is positioned 14° to the incidence of normalized frequency 0.25. The background is set to be Ge. The LC index is tuned as 1.8 for (a) and (b), and 2.2 for (c). A mesh with 50 nm unit size is created on the structure. Time step is set at 5×10^{-17} s.

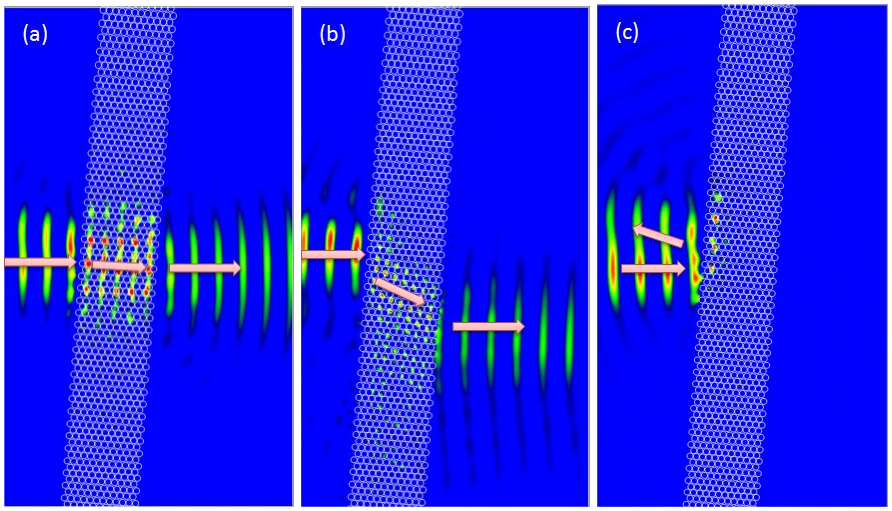

Figure 3.8 FDTD results of (a) positive refraction, (b) negative refraction, and (c) total reflection in hexagonal PhC slabs with Ge background.

3.3 In-plane tuning of anisotropic refractive index

In the configuration discussed above, the tuning is realized in the vertical direction. In this way, the propagation of in-plane light always experiences a homogeneous permittivity in LC in spite of the direction at which it is transmitting. The tuning can be described no more than raising or reducing the refractive index in the LC cells. The mathematical treating is relatively simple. In this part, with the introducing of otherwise in-plane ***E*** fields, anisotropy distinctively exerts its influence on the dispersive relationship. The high symmetry will be broken. The EFCs are expected to be deformed.

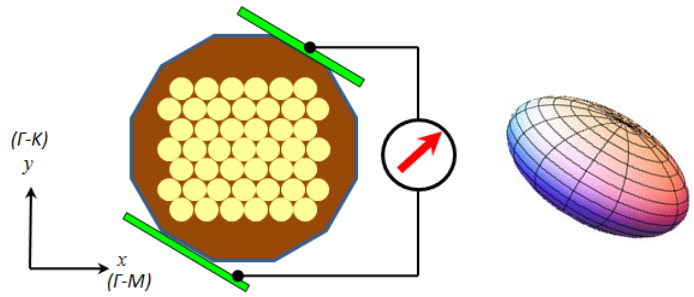

Figure 3.9 In-plane tuning of LC permittivity; The oblate index spheroid rotates in the plane.

To begin with, the external field is applied along the y axis, assuming the field induces saturation in the LC, *i.e.* (n_o, n_e) being (2.2, 1.6). Similar to the previous discussion, the TE modes, with E field only pointing perpendicular to the plane, will take no effect from the anisotropy. The LC index to this mode is independent of the direction of the wave vectors. For TM mode, the 6-fold rotational symmetry is broken. As a direct result, the high symmetry points K and M diverged to two subgroups M_1, M_2, K_1, and K_2. The $\boldsymbol{k}$ path Γ-M-K-Γ to depict a complete band structure is subject to adaption. The new path is suggested to be Γ-M_1-K_1-Γ-M_2-K_2-Γ, which is shown in fig 3.10. The corresponding band diagram for TM mode shows a discrepancy between the two paths, while for TE they degenerated. No band gap exists in either mode, as a difference from the perpendicular tuning scheme aforementioned. Still, this is due to the fact that the optical axis of LC is aligned along Γ-K. In more general cases where the axis is arbitrarily oriented, the $\boldsymbol{k}$ path has to cover at least half of these points, for there only exists the inverse symmetry.

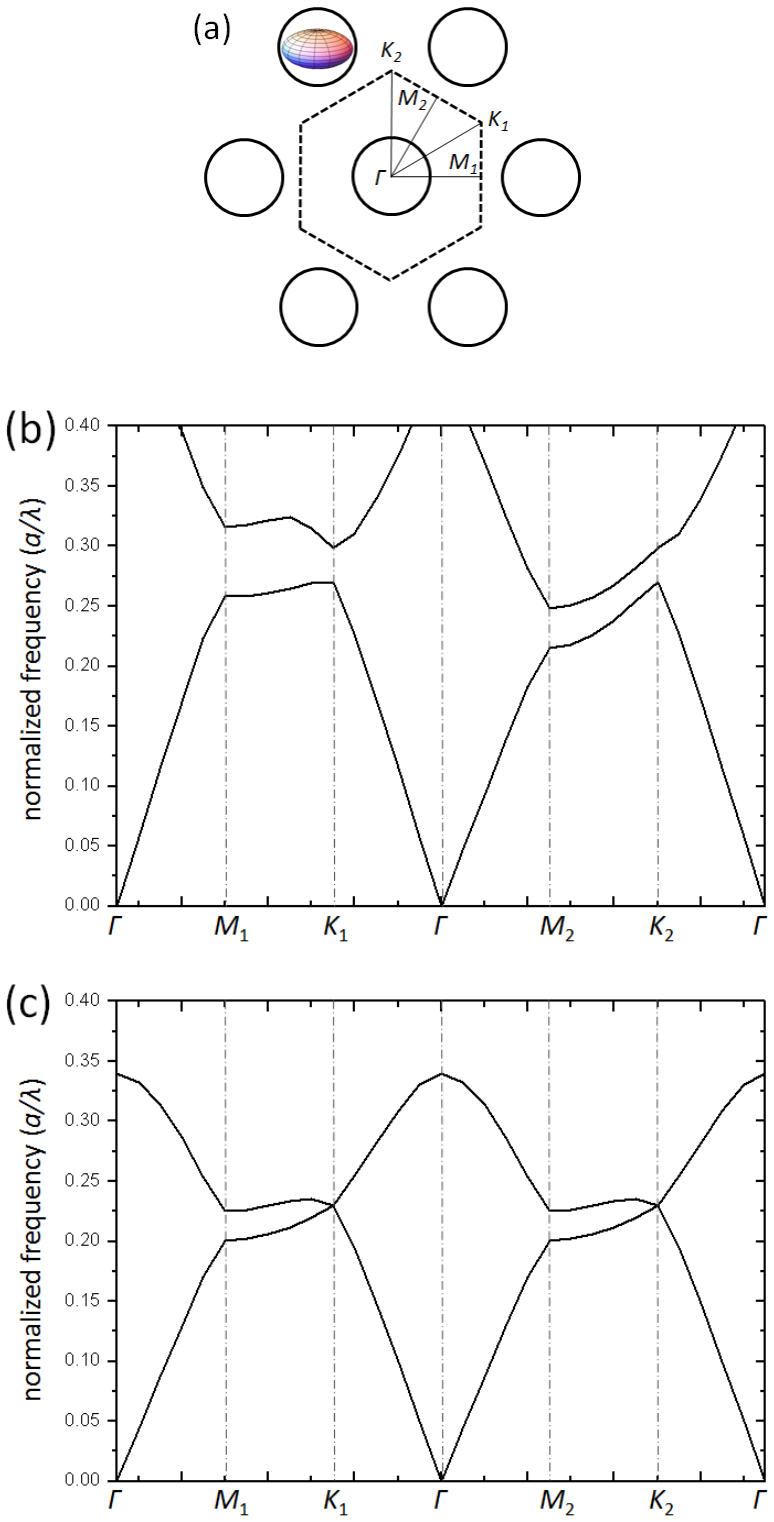

Figure 3.10 (a) The 6-fold rotational symmetry is broken in external E field. (b) TM diagrams diverge between the two $\boldsymbol{k}$ paths, while (c) TE ones remain the same.

EFCs could be a better way to investigate the anomaly opened by the anisotropy. In the direction of the LC optic axis, the wave propagation is subject to a raised n_e, thus the gradient of the contours becomes lower in the first band. The situation reverses in the second band, because the frequency rises inwardly there. As a result, the magnitude of wave velocity can be modulated in this way. The distorted EFCs also alter the refraction drastically. For example, given an incidence roughly along the *x* direction in the first band, the untuned structure will support a large refraction angle, owing to the fact that the first band of hexagonal structure has relative circular shape. After tuning along the *y* direction, the curves on the right fringe are much flatter. Incidence within a large range of angle will be gathered and collimated. The negative refraction taking place in the second band is strongly tuned, as well, in terms of the refraction angle and the threshold incident angle.

The beauty of in-plane tuning lies largely in the additional degree of freedom to change the tuning directions. The variety of the distorted EFCs increases significantly. For this hexagonal lattice, due to its high rotational symmetry, the directional tuning is restricted in 0° ~ 30°. However, the deformation of EFCs is remarkable, comparing with square lattice [34]. In Fig. 3.11(b), the negative refraction can be turned off in the second band by rotating the E field to Fig. 3.11(c), creating a partial band gap. By this method, an electrically controlled optical switch is realized. Meanwhile, the refraction angles in both bands can be continuously changed across a wide range.

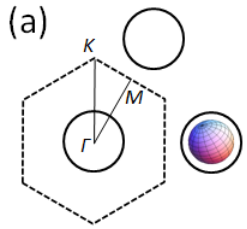
(a)
K
M
Γ

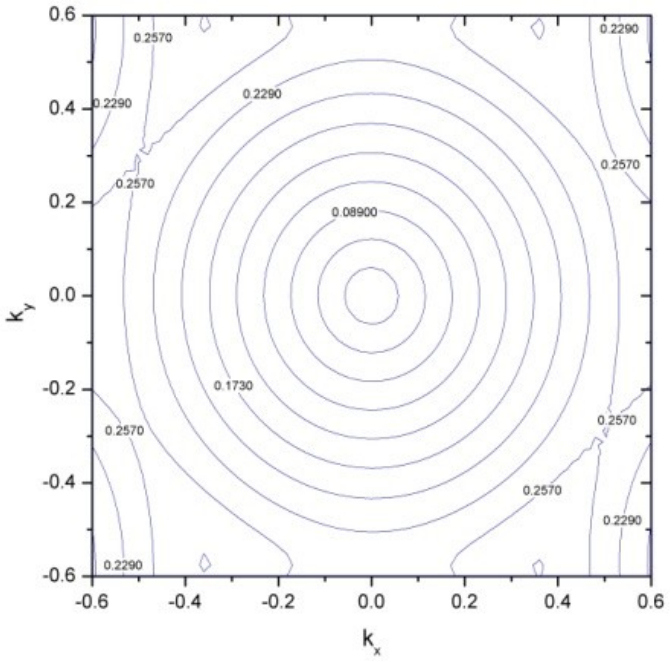
0.2570
0.2290
0.2290
0.2290
0.2570
0.2570
0.08900
0.1730
0.2570
0.2570
0.2570
0.2290
0.2290
0.6
0.4
0.2
0.0
-0.2
-0.4
-0.6
k_y
-0.6
-0.4
-0.2
0.0
0.2
0.4
0.6
k_x

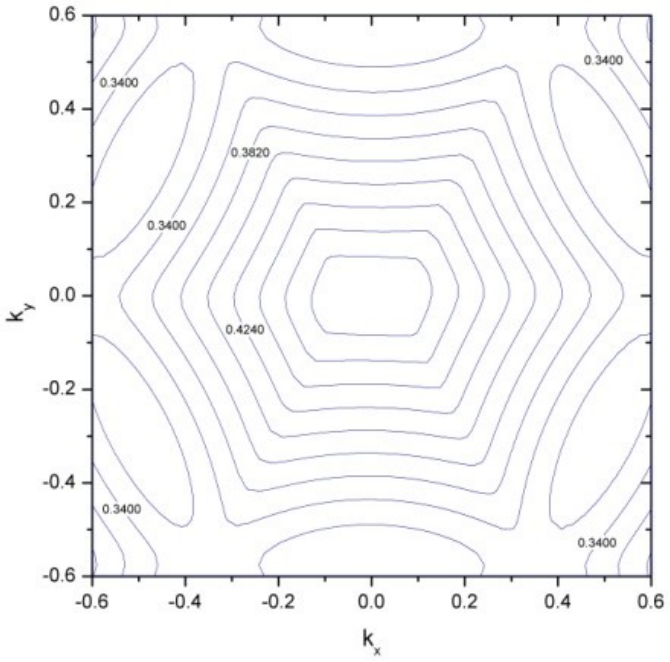
0.3400
0.3400
0.3820
0.3400
0.4240
0.3400
0.3400
0.6
0.4
0.2
0.0
-0.2
-0.4
-0.6
k_y
-0.6
-0.4
-0.2
0.0
0.2
0.4
0.6
k_x

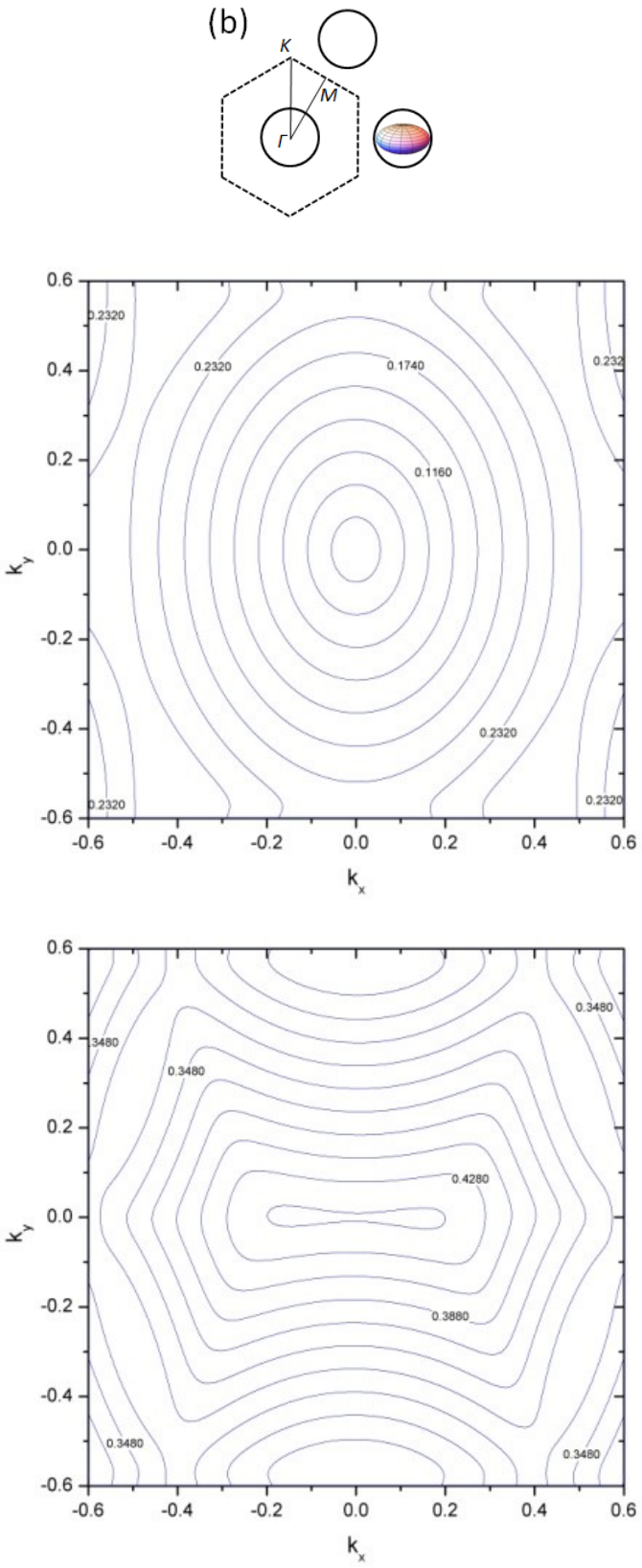
(b)
K
M
Γ
0.6
0.4
0.2
0.0
-0.2
-0.4
-0.6
k_y
k_x
0.2320
0.1740
0.1160
0.3480
0.4280
0.3880

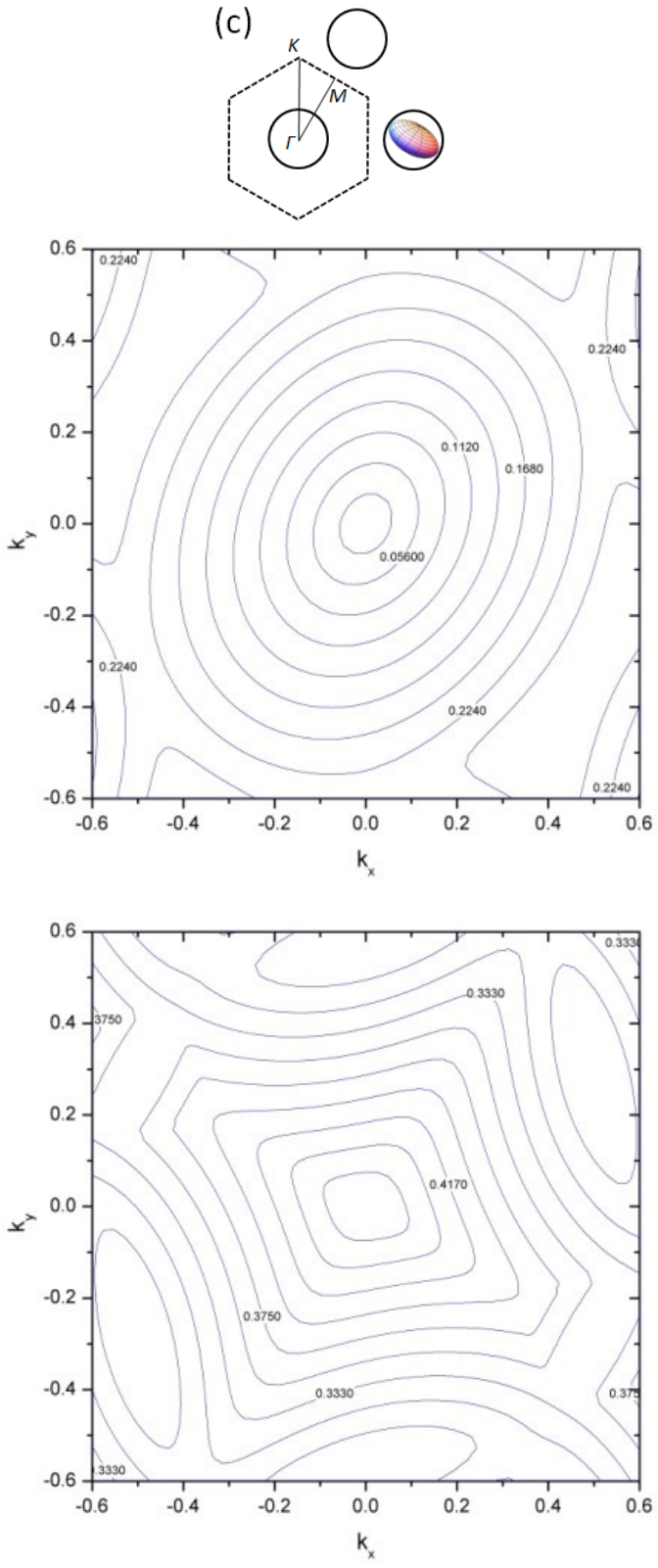
(c)
K
M
Γ
0.6
0.4
0.2
0.0
-0.2
-0.4
-0.6
k_y
k_x
0.2240
0.1120
0.1680
0.05600
0.3330
0.3750
0.4170
0.3330
0.3750
0.3330

Figure 3.11 EFCs of TM modes in the first and second bands, (a) without an external E field; (b), (c) with the E field applied along Γ-K and Γ-M, respectively.

The density of states (DOS) and local DOS (LDOS) mentioned in the previous chapter are particularly important to characterize the spontaneous emission in PhCs. Besides, DOS provides useful description of the mode distribution. Based on the theory discussed in chapter 2, the histogramming approach is introduced. The FBZ of hexagonal lattice is not very convenient to define in program. In regarding of this, calculation is carried out equivalent in the reciprocal primitive cell, which is discretized into a 51×51 mesh, i.e. 2601 points. The $\boldsymbol{k}$ points resolution Δk is hence determined as 0.02 with normalized frequency unit. The frequency resolution $\Delta\omega$ is also need to be determined according to (2.12). However, the gradient of frequency varies in different bands and locations in the reciprocal space. Examination shows that EFCs in the first band have large slope, and the distribution is relatively homogenous. A rough estimation of the maximum is therefore made around 0.5. Combined with Δk, the histogram bins, i.e. $\Delta\omega$, are set at 0.01. Data is sampled in the first 6 bands (Fig. 3.12).

(a) DOS

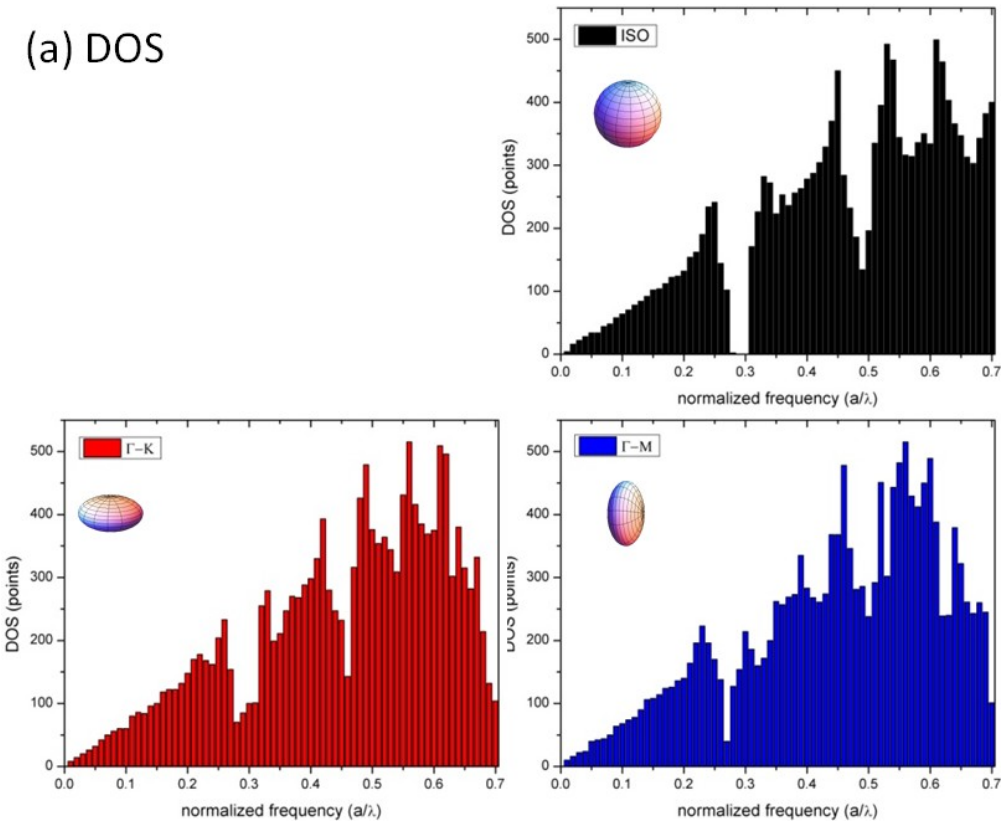

(b) LDOS@apex

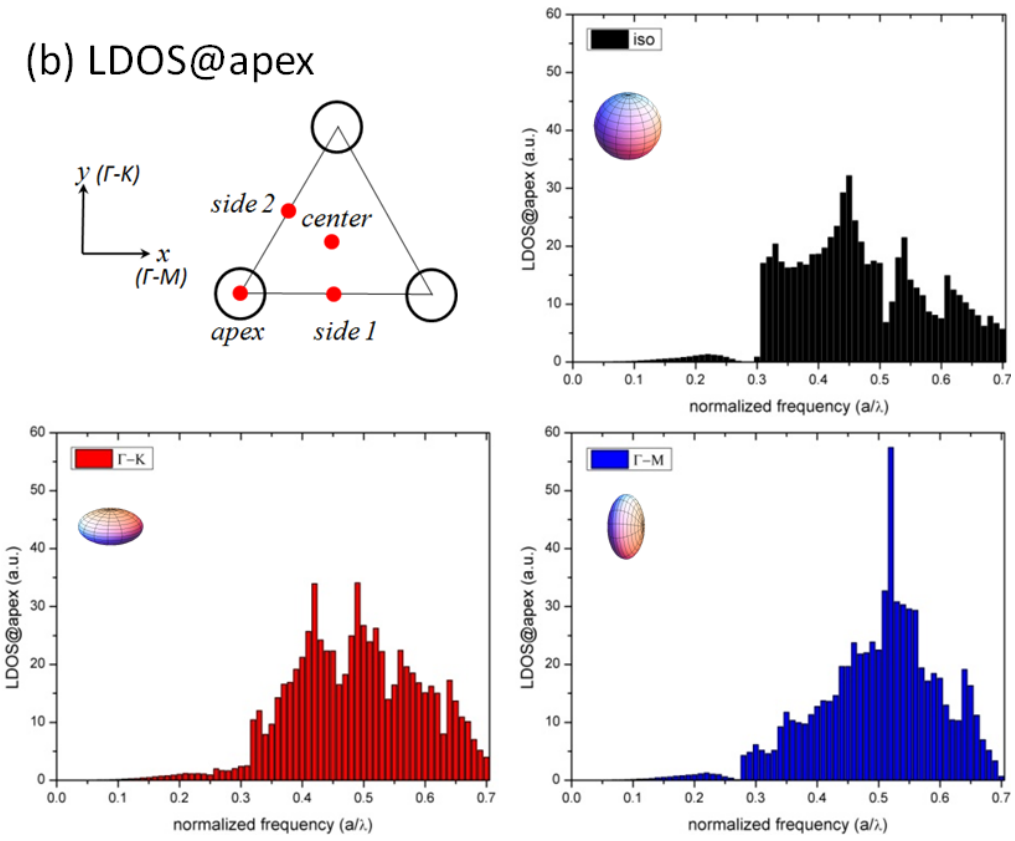

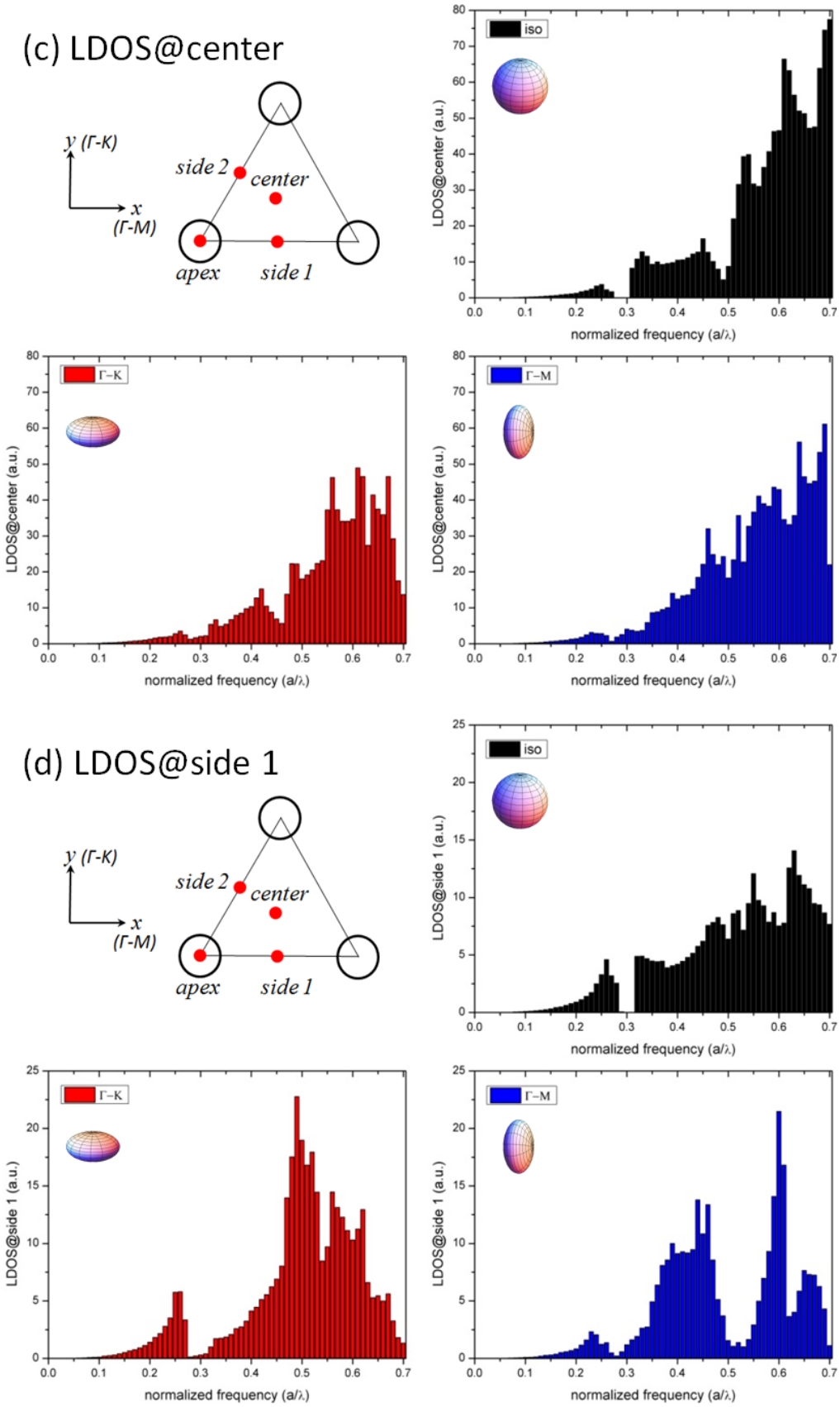
(c) LDOS@center
y (Γ-K)
x (Γ-M)
side 2
center
apex
side 1
ISO
Γ−K
Γ−M
LDOS@center (a.u.)
normalized frequency (a/λ)
(d) LDOS@side 1
LDOS@side 1 (a.u.)

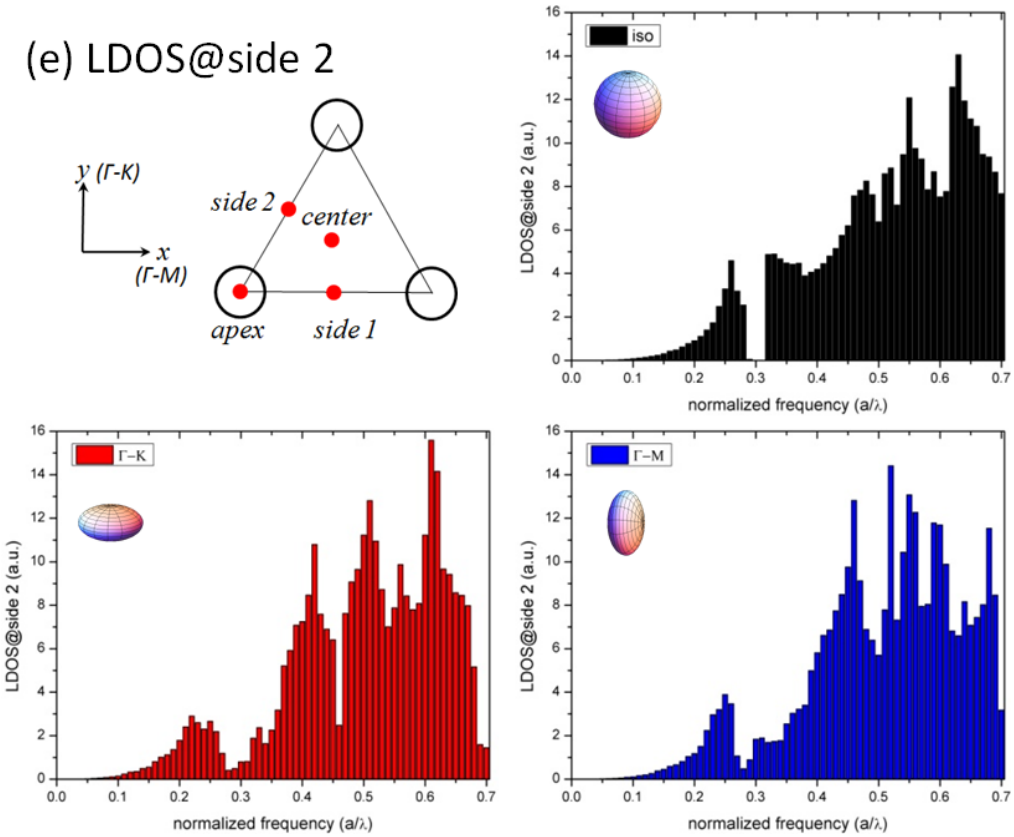

Figure 3.12 (a) DOS and (b-e) LDOS calculated for two dimensional hexagonal PhC at (b) central area of the holes, (c) center of the triangle formed by 3 neighboring holes, (d, e) mid points of two different sides of the triangle.

A complete band gap around frequency 0.28 is clearly shown in fig 3.12 (a) for the untuned situation. The saturation tuning applied on two directions both cancel the gap. However a dip can still be located. Correspondingly, dips around 0.28 in each LDOS chart for different locations can be found. Large DOS does not guarantee large LDOS since the later is the product of DOS and electric field intensity. Either part will lead to the difference. The LDOS projected on the center of LC holes (*apex*) and center of a triangular formed by three holes (*center*) are significantly larger than those on the mid points between two holes (*side 1, 2*).

In the low-frequency range, mostly in the first band, the field strength is weak, represented by low LDOS. A step-like profile could be observed in vicinity of the first band edge. The LDOS at *apex* and *center* are significantly larger than those on the *sides*, indicating that high field intensity can be expected.

The spikes and dips in LDOS diagram indicate potential enhancement and suppression of quantum optical effects. In tuned results, the DOS and LDOS profiles seem spikier. This could be an indication of the modified field distribution. Also, the distorted EFCs could lower the frequency resolution by changing the group velocity according to (2.12). Noise peaks and dips could be introduced.

It is noteworthy that all the quantities in the calculation are dimensionless. The results can be scaled to fit in practical structure design.

References

[1] G. Alagappan, X.W. Sun, P. Shum, and M.B. Yu, "Engineering the bandgap of a two-dimensional anisotropic photonic crystal," *Journal of the Optical Society of America B*, vol. 23, 2006, p. 1478.

[2] D. Prather, S. Shi, J. Murakowski, and GJ, "Self-collimation in photonic crystal structures: a new paradigm for applications and device development," *Journal of Physics D:*, vol. 40, 2007, p. 2635.

[3] H. Kosaka, T. Kawashima, A. Tomita, M. Notomi, and T, "Self-collimating phenomena in photonic crystals," *Applied Physics*, 1999.

[4] M. Notomi, "Theory of light propagation in strongly modulated photonic crystals: Refractionlike behavior in the vicinity of the photonic band gap," *Physical Review B*, vol. 62, 2000, pp. 10696-10705.

[5] C. Luo, S.G. Johnson, and J.D. Joannopoulos, "All-angle negative refraction in a three-dimensionally periodic photonic crystal," *Applied Physics Letters*, vol. 81, 2002, p. 2352.

[6] S. Foteinopoulou and C. Soukoulis, "Negative refraction and left-handed behavior in two-dimensional photonic crystals," *Physical Review B*, vol. 67, 2003, pp. 1-5.

[7] S. Foteinopoulou, E. Economou, and C. Soukoulis, "Refraction in media with a negative refractive index," *Physical review letters*, vol. 90, 2003, p. 107402.

[8] C. Luo, S. Johnson, J. Joannopoulos, and J. Pendry, "Negative refraction without negative index in metallic photonic crystals.," *Optics express*, vol. 11, 2003, pp. 746-54.

[9] R. Moussa, S. Foteinopoulou, L. Zhang, G. Tuttle, K. Guven, E. Ozbay, and C. Soukoulis, "Negative refraction and superlens behavior in a two-dimensional photonic crystal," *Physical Review B*, vol. 71, 2005, pp. 1-5.

[10] J. Pendry, "Negative refraction makes a perfect lens," *Physical review letters*, vol. 85, 2000, pp. 3966-9.

[11] D. Smith, W. Padilla, D. Vier, S. Nemat-Nasser, and S. Schultz, "Composite medium with simultaneously negative permeability and permittivity," *Physical review letters*, vol. 84, 2000, pp. 4184-7.

[12] J. Pendry, A. Holden, W. Stewart, and I. Youngs, "Extremely low frequency plasmons in metallic mesostructures.," *Physical review letters*, vol. 76, 1996, pp. 4773-4776.

[13] a. Berrier, M. Mulot, M. Swillo, M. Qiu, L. Thylén, a. Talneau, and S. Anand, "Negative Refraction at Infrared Wavelengths in a Two-Dimensional Photonic Crystal," *Physical Review Letters*, vol. 93, 2004, pp. 1-4.

[14] H. Chien, H. Tang, C. Kuo, C. Chen, and Z. Ye, "Directed diffraction without negative refraction," *Physical Review B*, vol. 70, 2004, pp. 2-5.

[15] T. Ding, K. Song, K. Clays, and C. Tung, "Fabrication of 3D Photonic Crystals of Ellipsoids: Convective Self-Assembly in Magnetic Field," *Advanced Materials*, vol. 21, 2009, pp. 1936-1940.

[16] I. Hosein and C. Liddell, "Convectively assembled nonspherical mushroom cap-based colloidal crystals," *Langmuir*, 2007.

[17] K.P. Velikov, T. van Dillen, A. Polman, and A. van Blaaderen, "Photonic crystals of shape-anisotropic colloidal particles," *Applied Physics Letters*, vol. 81, 2002, p. 838.

[18] W. Yuan, L. Wei, T.T. Alkeskjold, A. Bjarklev, and O. Bang, "Thermal tunability of photonic bandgaps in liquid crystal infiltrated microstructured polymer optical fibers.," *Optics express*, vol. 17, 2009, pp. 19356-64.

[19] J. Hwang, M.H. Song, B. Park, S. Nishimura, T. Toyooka, J.W. Wu, Y. Takanishi, K. Ishikawa, and H. Takezoe, "Electro-tunable optical diode based on photonic bandgap liquid-crystal heterojunctions.," *Nature materials*, vol. 4, 2005, pp. 383-7.

[20] S. Xiong and H. Fukshima, "Analysis of light propagation in index-tunable photonic crystals," *Journal of Applied Physics*, vol. 94, 2003, p. 1286.

[21] D. Scrymgeour, N. Malkova, S. Kim, and V. Gopalan, "Electro-optic control of the superprism effect in photonic crystals," *Applied Physics Letters*, vol. 82, 2003, p. 3176.

[22] J. Weirich, J. Laegsgaard, L. Wei, T.T. Alkeskjold, T.X. Wu, S. Wu, and A. Bjarklev, "Liquid crystal parameter analysis for tunable photonic bandgap fiber devices.," *Optics express*, vol. 18, 2010, pp. 4074-87.

[23] T. Alkeskjold, J. Lægsgaard, A. Bjarklev, D. Hermann, A. Anawati, J. Broeng, J. Li, and S. Wu, "All-optical modulation in dye-doped nematic

liquid crystal photonic bandgap fibers.," *Optics express*, vol. 12, 2004, pp. 5857-5871.

[24] L. Scolari, T. Alkeskjold, J. Riishede, A. Bjarklev, D. Hermann, A. Anawati, M. Nielsen, and P. Bassi, "Continuously tunable devices based on electrical control of dual-frequency liquid crystal filled photonic bandgap fibers.," *Optics express*, vol. 13, 2005, pp. 7483-96.

[25] F. Du, Y. Lu, and S. Wu, "Electrically tunable liquid-crystal photonic crystal fiber," *Applied Physics Letters*, vol. 85, 2004, p. 2181.

[26] M. Haakestad, T. Alkeskjold, M. Nielsen, L. Scolari, J. Riishede, H. Engan, and a. Bjarklev, "Electrically tunable photonic bandgap guidance in a liquid-crystal-filled photonic crystal fiber," *IEEE Photonics Technology Letters*, vol. 17, 2005, pp. 819-821.

[27] T.R. Wolinski, K. Szaniawska, S. Ertman, P. Lesiak, a.W. Domanski, R. Dabrowski, E. Nowinowski-Kruszelnicki, and J. Wojcik, "Influence of temperature and electrical fields on propagation properties of photonic liquid-crystal fibres," *Measurement Science and Technology*, vol. 17, 2006, pp. 985-991.

[28] T. Larsen, A. Bjarklev, D. Hermann, and J. Broeng, "Optical devices based on liquid crystal photonic bandgap fibres.," *Optics express*, vol. 11, 2003, pp. 2589-96.

[29] a. Lorenz, H. Kitzerow, a. Schwuchow, J. Kobelke, and H. Bartelt, "Photonic crystal fiber with a dual-frequency addressable liquid crystal: behavior in the visible wavelength range.," *Optics express*, vol. 16, 2008, pp. 19375-81.

[30] K. Busch and S. John, "Liquid-Crystal Photonic-Band-Gap Materials: The Tunable Electromagnetic Vacuum," *Physical Review Letters*, vol. 83, 1999, pp. 967-970.

[31] H. Takeda and K. Yoshino, "Tunable photonic band schemes of opals and inverse opals infiltrated with liquid crystals," *Journal of Applied Physics*, vol. 92, 2002, p. 5658.

[32] J. Joannopoulos, S. Johnson, J. Winn, and R. Meade, *Photonic crystals: molding the flow of light*, Princeton Univ Pr, 2008.

[33] H. Wang, "Fabrication, characterization, and simulation of photonic bandgap structures," *East*, 2009.

[34] Y. Wang and L. Chen, "Tunable negative refraction photonic crystals achieved by liquid crystals.," *Optics express*, vol. 14, 2006, pp. 10580-7.

CHAPTER 4

Analyses in Three-Dimensional PhCs

In previous chapters, a range of novel phenomena and promising applications in PhCs have been mentioned. Many of these traits stem in the unique anisotropic nature of this material, which fundamentally reshapes the behaviors of the light propagation, such as beam shaping and super collimation. The active researches of negative refraction have also led to a great expectation of its realization in PhCs, due to its capacity to maneuver the electromagnetic waves. However, the delicacy of such structures has also set barriers. On one hand, difficulties have been met to apprehend the properties and functions. Fundamentally, it is vital to precisely describe the distribution and evolution of EM fields. Beside the effort of recognition, PhCs impose tight requirements on designing and fabrication referring to the delicate structural parameters. Thus effective analytical tools are highly desirable to efficiently design and optimize the PhCs structures. Great efforts have been made into the exploration. Until recently, researches have been mostly focused on two-dimensional (2D) structures, and the progresses have been acknowledged. However, there are intrinsic limitations in the 2D systems. Super collimation, perfect lens, and many other refraction based phenomena could only achieve their full functionality in three-dimensional (3D) structures [1,2]. Therefore, the investigation of light refraction in 3D PhCs is of special importance. The task still remains largely a challenge. Apart from the difficulties from the aspects of fabrication and experimentation, theoretical analysis is complicated and suffers from many restrictions, although in principle, the paradigm is similar to 2D situations.

Despite the difficulties, efforts have been pooled to illustrate the intriguing spatial structures. A case of 3D all-angle negative refraction (AANR) was discussed by C. Luo, *et al*. [3]. The light focusing and self-collimation were also discussed in 3D structures [2,4,5]. On the other hand, Xiaonan Chen, *et al*., have made contribution in the aspect of theoretical study [3]. In this part, the work deals with the theoretical analysis of 3D PhCs.

4.1. Refraction analysis in 3D PhC

Given the particular importance to investigate the light refraction in 3D PhCs, an analysis procedure is developed for a clearer and more simplified picture for light refraction and propagation in 3D PhCs, especially with the capability of identifying the negative refraction. The method can be readily applied to other lattice structures.

The demonstration PhC is modeled in Fig. 4.1 as a face-center cubic (FCC) lattice, with the lattice constant a being 1 in the normalized unit. Air filled spherical cavities with a radius of 0.353 are fitted in the lattice, so that they are tightly packed, with the filling ratio of $r/a = 0.353$. The spheres are surrounded by silicon background. The structure is also called as an inverse opal. These two materials are assumed both homogenous and non-dispersive. To begin with, the calculation of the dispersion relation is carried out in the reciprocal space (the wave vector space), in which each $\boldsymbol{k}$ point stands for a wave vector. Calculation dimension is limited to the first Brillouin zone, which for FCC is an *Octahedron*. For simplicity,

a cubic space with sides of normalized length 1 is chosen. The cube is discretized into a ***k*** points array.

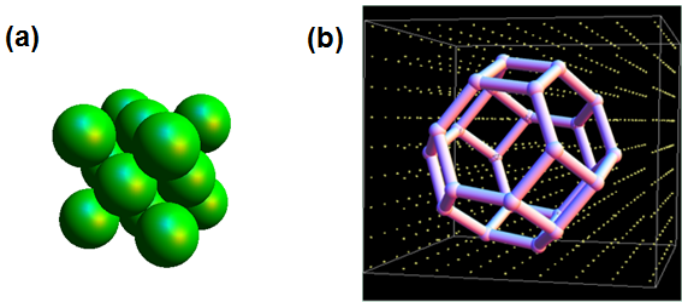

Figure 4.1 The air-cavity FCC lattice in silicon background with r/a = 0.353: (a) the structure in real space and (b) the first Brillouin Zone with a shape of a truncated octahedron.

PWE algorithm is implemented on each point to find out the eigenfrequencies. Following the same procedures in 2D situation, three-dimensional equifrequency surfaces (EFSs) can be plotted for each band, by interpolating and linking ***k*** points of similar frequency. The resolution of 3D PWE is set as 24 mesh steps in each dimension with an err tolerance of 5×10^{-6}. EFSs for the first, the third, and the fifth bands are shown in Fig. 4.2 together with the band diagram. All the three bands are of TE mode. It is noteworthy that the diagram is a hybrid of the TE and TM modes. The definition is inherited from the two-dimensional PWE in the previous chapter, while different from the work of the MIT group [6]. The modes with magnetic fields lying in the *x*-*y* plane are named as TE, while electric field in the plane is called TM mode.

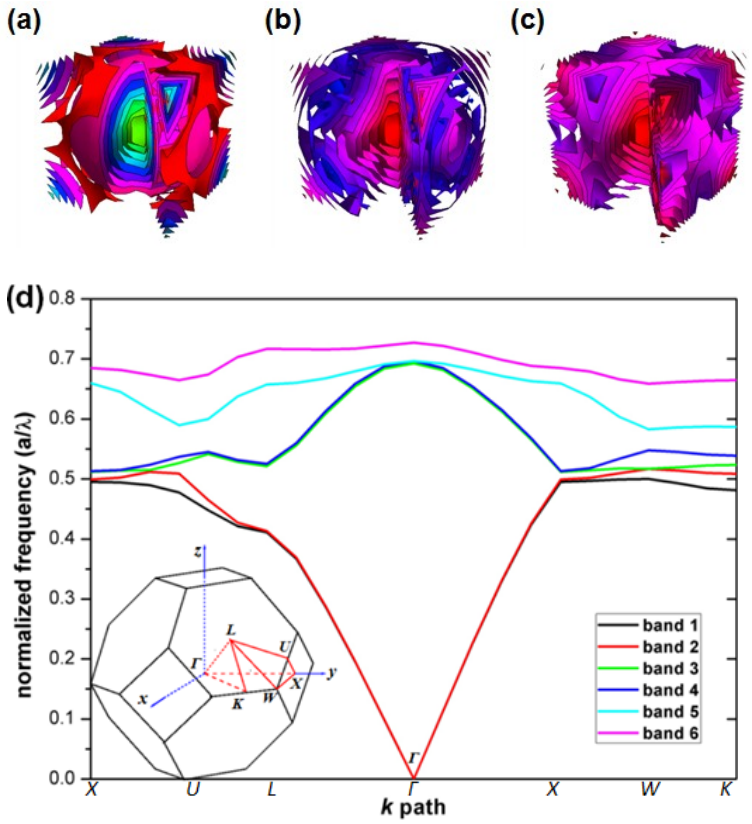

Figure 4.2. The EFSs of (a) the first, (b) the third, and (c) the fifth bands covering the first Brillouin zone for isotropic inverse opal structure, with frequencies being differentiated by the pseudo color codes. In the first band, the outgoing direction generally coincides with rising frequency, while this trend reverses in the third band. (d) The band diagrams of the first 6 bands are shown, along ***k*** path *X*-*U*-*L*-*Γ*-*X*-*W*-*K*.

In Fig. 4.2, all three bands turn on a sphere-like shape in the inner zone, in vicinity of the origin point. This can be clearly related to the central part in the band diagram (Fig. 4.2(d)), where the curves are monotonic. However, in outer part, as well as in the upper bands, the diagram curves are undulate, which is also reflected by more distorted EFSs. The group velocity for a specific wave vector ***k*** (a point in the reciprocal space) can be deduced geometrically from the gradient

vector of local EFS of frequency ω. Given the shapes of the EFSs, the refraction information could be thereby extracted theoretically. Note the dispersion curve at the third band in the vicinity of the center point in Fig. 4.2(d), a convex shape with a negative slope could be found, implying a possible place where negative refraction takes place. Its three-dimensional counterpart is explicitly shown as the convex EFSs in the central third band in Fig. 4.2(b). The spherical shape acts as a potential candidate for AANR and super lens.

The 3D EFSs, though have provided thorough details throughout the Brillouin zone, are not as convenient to provide an intuitive view as in 2D situations. On the other hand, the resource and time cost are demanding to provide extra information for the additional dimension. To solve address this challenge, a direct 2D analysis is proposed on a specified cross section of the EFSs, which usually represents the incident plane. In this demonstration, the set of 24×24×24 points in the 3D space is significantly reduced to 40×40 points on a 2D plane. An improved resolution is enabled by utilizing the spared cost for the third dimension. The scheme is illustrated in Fig. 4.3. An incident plane is decided first, and then followed by a direct 3D analysis. The contour details are quite restricted by the calculation resolution, as shown in Fig. 4.3(b). Instead, points could be sampled from the predefined plane in the first place. The two-dimensional EFCs are directly plotted without taking into account of the irrelevant part, saving time and resources. Next, the study will be performed in the detail-improved 2D EFCs.

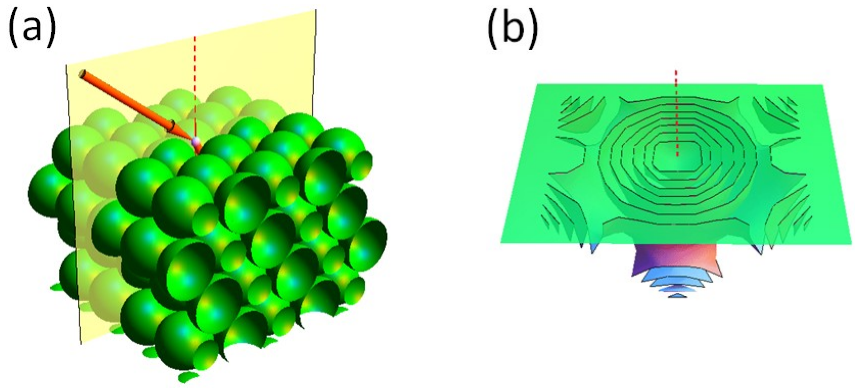

Figure 4.3. (a) The schematic diagram of light incidence on an FCC photonic crystal interface of (111). The arrow denotes the incident beam, lying in the incident plane (denoted by the yellow plane). (b) A cross section of the dissected 3D EFSs in the first band by the incident plane (denoted by the green plane).

Fig. 4.4 presents two sets of EFCs on planes (111) and (123), assuming the vertical directions of both figures are along the normal line of the interface. Black dashed lines denote the normal lines. The incidences come from the upper left, with their wave vectors pointing towards lower right. With the conservation of the parallel wave vector, the wave vector of refracted lights in PhC should have the same parallel component. This limitation is denoted by the white dashed lines. In Fig. 4.4, both wave vectors of refracted lights are determined, directing from the center point towards upper right. Subsequently, the projections of the refractions inside the incident plane (group velocities in blue arrows) are defined respectively by the patterns of the EFCs. It turns out both negative refractions at normalized frequency of 0.6205 are identified in these schemes of incidence. Moreover, the convex inner contours on these two different slices imply focusing behavior may happen in the three dimensional structure in this frequency range.

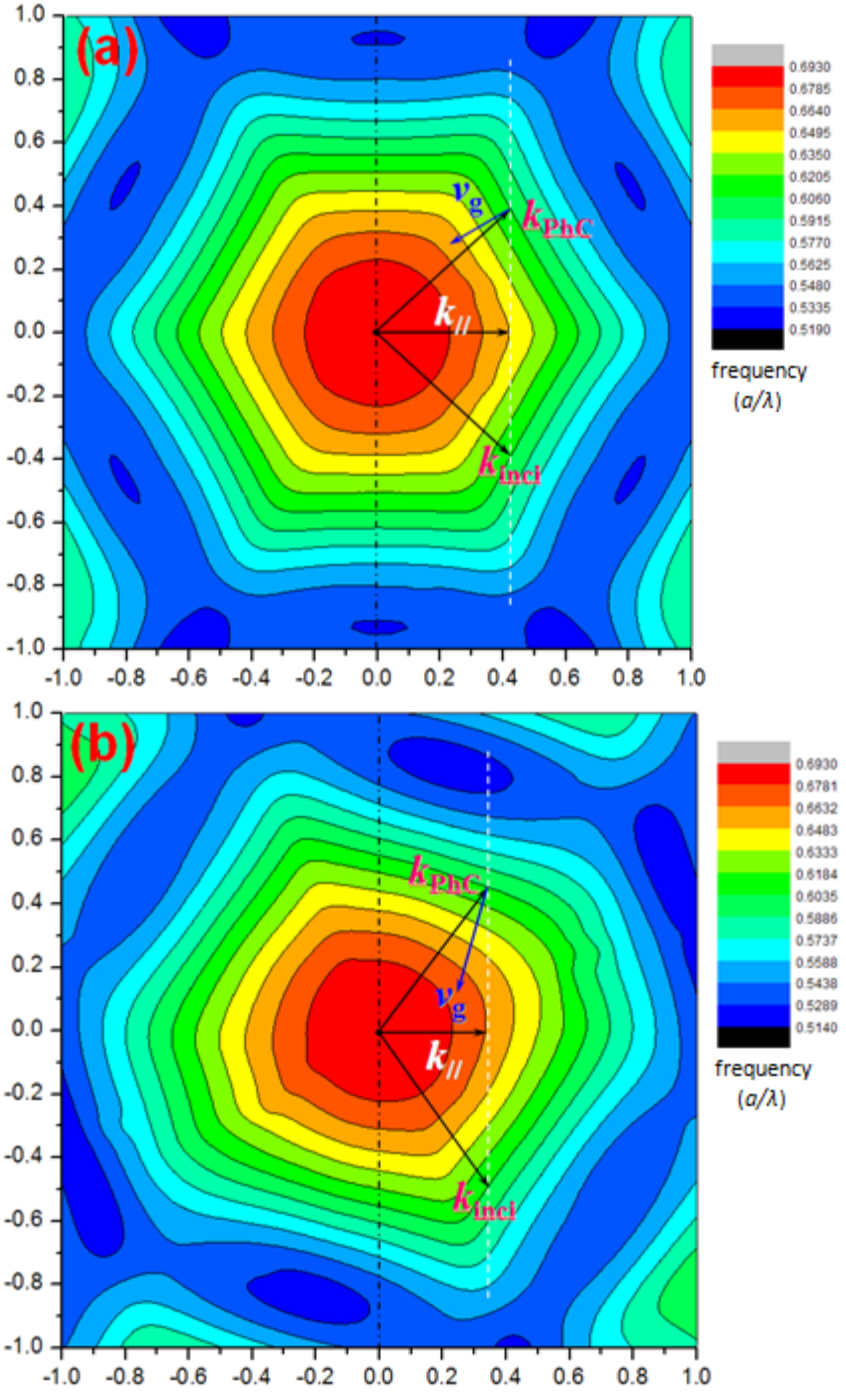

Figure 4.4. 2D EFCs in plane (a) (111) and (b) (123) of the third band; assuming the horizontal direction lies in the interface, negative refractions exist with respect to the dashed normal vector; the normal lines are denoted by black dashed lines; the blue arrows show projection of refractions on the incident plane.

From the EFSs displayed above, the effective refractive index n_{eff} can be obtained, which could be used in the Snell's law to numerically predict the refraction angle. Assuming the light is incident from air, Fig. 4.5 gives n_{eff} as a function of (1) frequency with incident angle fixed at 45°, and (2) incident angle with frequency 0.5886, for which refraction on these two planes majorly appears negative.

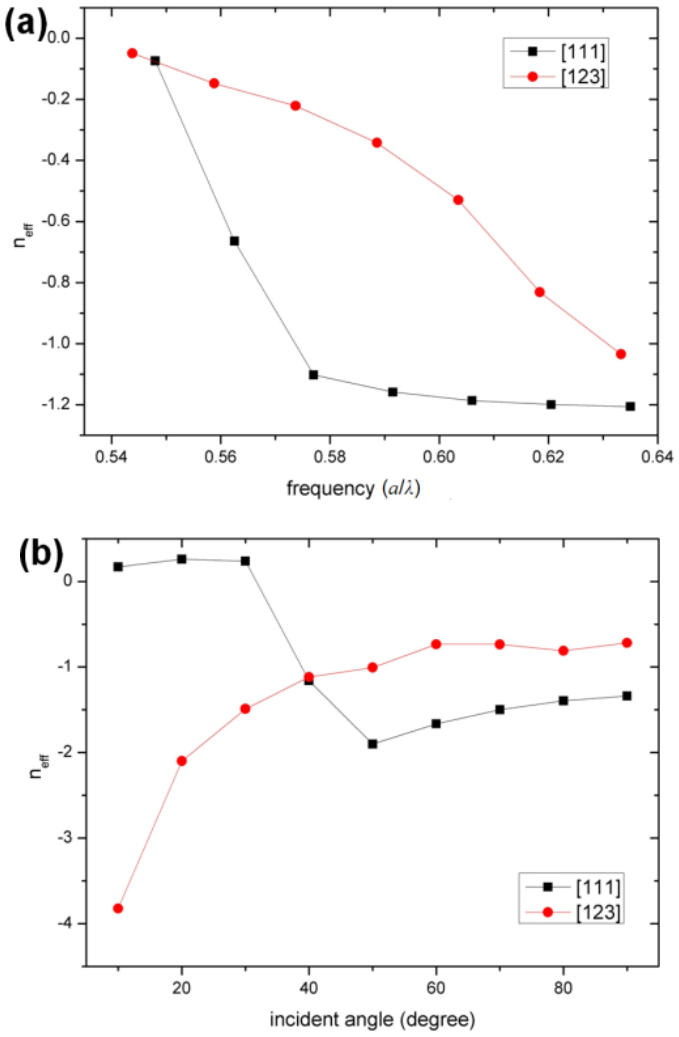

Figure 4.5 Effective refractive index vs. (a) the frequency with fixed incident angle of 45°, and (b) incident angle at frequency 0.5886, in the third band.

The EFCs on cross section planes show similarity to those of 2D PhCs. Though,

there are significant differences brought by the extra dimension. 3D PhCs are highly anisotropic structures, thus mirror symmetry is usually restricted in a few special locations. As a result, it is not common the incident plane intersects with the EFSs perpendicularly. The group velocities thereby deviate from the incident plane. For example, plane (111) is of mirror symmetry, and the light propagation will stick in the incident plane. The analysis hence is no different from that in 2D PhCs. While this is not the case for plane (123), the out-of-plane component will emerge inevitably. Based on this method, the refraction can be still efficiently determined in any 3D PhCs.

4.3 Tunable three-dimensional PhCs

In this part, nematic-liquid-crystal-infilled three-dimensional PhCs with FCC structure is investigated. The birefringence model of LC has been introduced in the plane wave expansion method. With the help of this model, the tuning effect of external electric field can be visualized in the deformation of EFSs. The emerging anisotropy strongly alters the characters of the PhCs, leading to a variety of potential applications, such as optical switch and tunable cavities.

Given the anisotropic permittivity in 3D system, a three-rank tensor should be taken into account. Calculation usually involves extreme complexity, because the orientation of the polarized LC is arbitrarily determined by the external field. Following the introduction in chapter two, a rotation transformation is introduced to circumvent this difficulty. The idea is shown in Fig. 4.6.

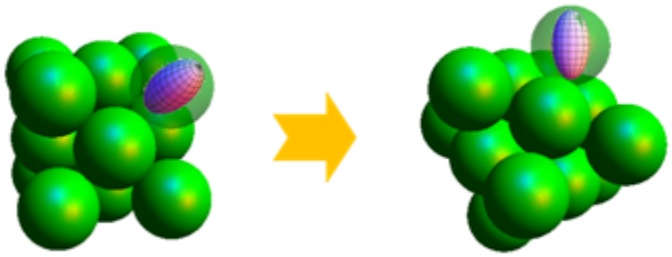

Figure 4.6 LC infill inverse opal structure; silicon background with r/a = 0.353. The uni-axial LC is rotated to sit normally in the computation coordinates.

In Fig. 4.6, LC infill is injected into the air cavities of the previous FCC PhC. External filed can be applied in arbitrary directions. The LC is assumed to have isotropic refractive index n_0 = 1.8, and anisotropic index in saturation (n_e, n_o) = (2.7, 1.5), respectively. Thus this is a positive axial material. An example case with $\boldsymbol{E}$ field along (123) direction is analyzed without loss of generality. The rotation transformation can be expressed as,

$$\boldsymbol{Q} = \begin{pmatrix} (56+3\sqrt{14})/70 & (-14+3\sqrt{14})/35 & -1/\sqrt{14} \\ (-14+3\sqrt{14})/35 & (7+6\sqrt{14})/35 & -\sqrt{2/7} \\ 1/\sqrt{14} & \sqrt{2/7} & 3/\sqrt{14} \end{pmatrix}, \qquad (4.1)$$

The rotated base vectors are hence determined as,

$$\boldsymbol{G_{new}} = (\boldsymbol{a_1' a_2' a_3'}) = \boldsymbol{QG} = \boldsymbol{Q}(\boldsymbol{a_1 a_2 a_3}) = \boldsymbol{Q}\begin{pmatrix} 0.5 & 0.5 & 0 \\ 0 & 0.5 & 0.5 \\ 0.5 & 0 & 0.5 \end{pmatrix}$$

$$= \begin{pmatrix} 0.346548 & 0.440535 & -0.173274 \\ -0.306904 & 0.38107 & 0.153452 \\ 0.534522 & 0.400892 & 0.668153 \end{pmatrix} \qquad (4.2)$$

Degeneracy no longer exists for high symmetry points on the BZ boundaries. In other words, band diagram along the previous $\boldsymbol{k}$ path could not give the correct band structure. The inverse symmetry is the only symmetry element that helps

simplify the calculation. To find out the correct band gap, half of the FBZ has to be scanned. The idea is shown in Fig. 3.7(b), where the external field saturates the index pair at $n_e = 2.7$, $n_o = 1.5$.

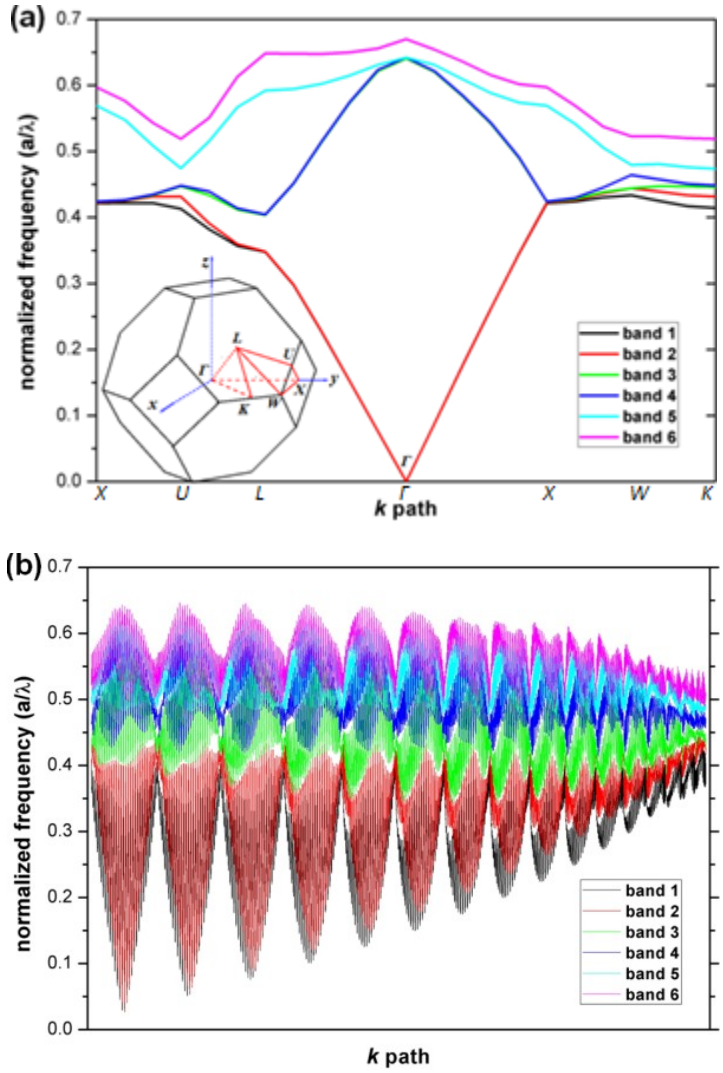

Figure 4.7 (a) Band diagram of LC-infill-silicon-backbone fcc without external electric field. (b) The exhaustive sampling in half FBZ shows no band gap exists in the first six bands.

Figs. 4.8(a-d) present the deformation of the first band EFSs as the external field tuning up to E_{sat} along direction (123). The spherical inner EFSs gradually turn into oval-like shapes. EFSs compressing happens along the external field where n_e grows, while bulging in the perpendicular directions can also be observed.

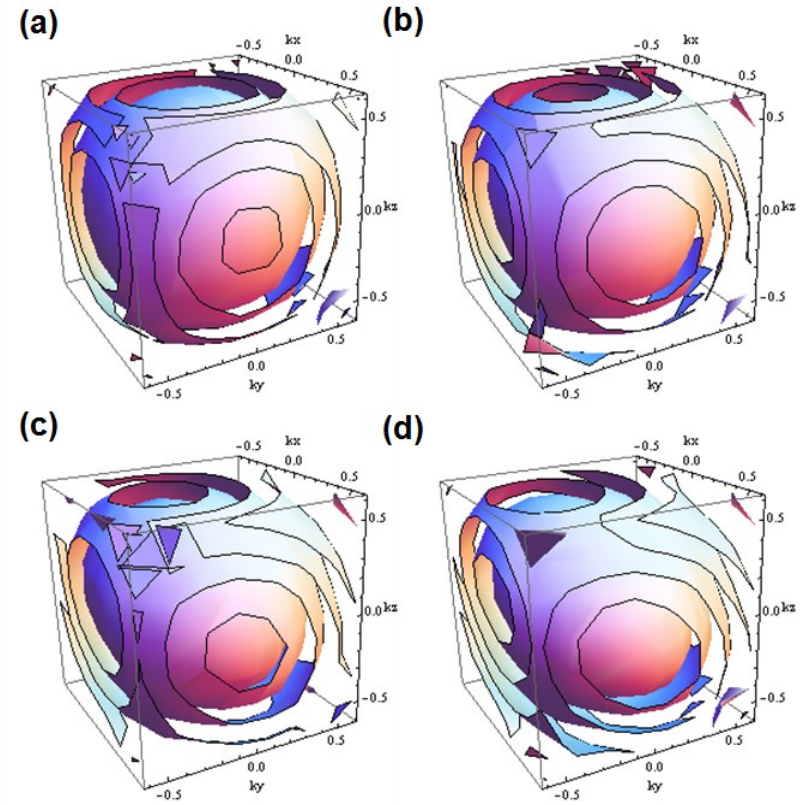

Figure 4.8 The EFSs of the first band of a series of refractive indices: (a) (1.9, 1.77), (b) (2.1, 1.7), (c) (2.4, 1.62), and (d) (2.7, 1.5); the electric field is applied along the orientation of (123). The compressing effect is clearly revealed.

A contrast of EFCs on different cross sections between the untuned and saturated LC models is shown in Fig. 4.9. Distortion of EFSs in the first band is slight, indicating less sensitiveness to anisotropy of the lower frequency modes. There are large sphere-like inner EFSs in this band. The PhC would act more like a

homogenous medium for light in this frequency range. The contours shape on the (123) cross section remains largely unchanged, which is perpendicular to the tuning field. The third band undergoes much severe deformation, because the shorter the wavelength, the more phase shift it would experience in a given distance. Since the negative refraction largely relies on this band, strong tuning effect could be achieved.

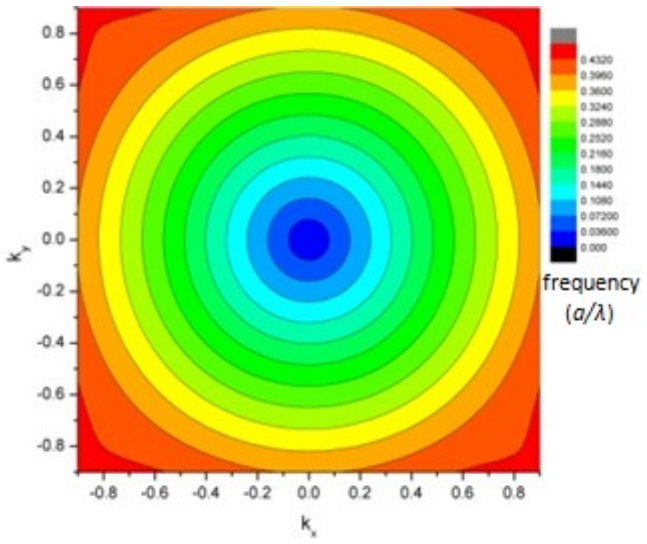
0.8
0.6
0.4
0.2
0.0
-0.2
-0.4
-0.6
-0.8
k_y
-0.8 -0.6 -0.4 -0.2 0.0 0.2 0.4 0.6 0.8
k_x
0.4320
0.3960
0.3600
0.3240
0.2880
0.2520
0.2160
0.1800
0.1440
0.1080
0.07200
0.03600
0.000
frequency
(a/λ)

(a)

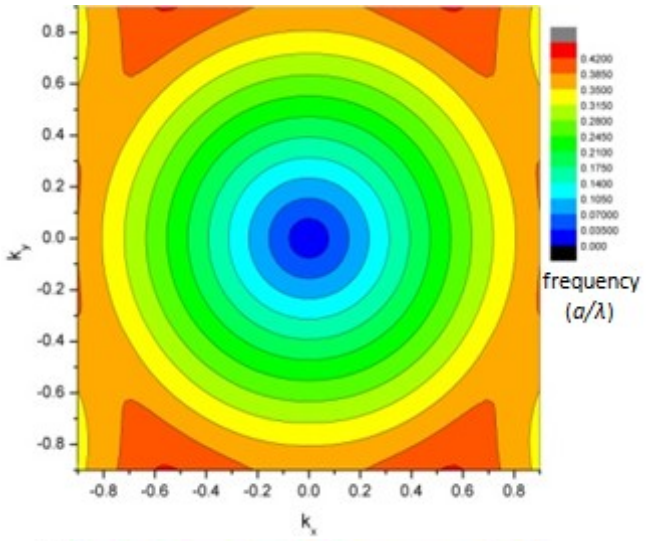
0.8
0.6
0.4
0.2
0.0
-0.2
-0.4
-0.6
-0.8
k_y
-0.8 -0.6 -0.4 -0.2 0.0 0.2 0.4 0.6 0.8
k_x
0.4200
0.3850
0.3500
0.3150
0.2800
0.2450
0.2100
0.1750
0.1400
0.1050
0.07000
0.03500
0.000
frequency
(a/λ)

(b)

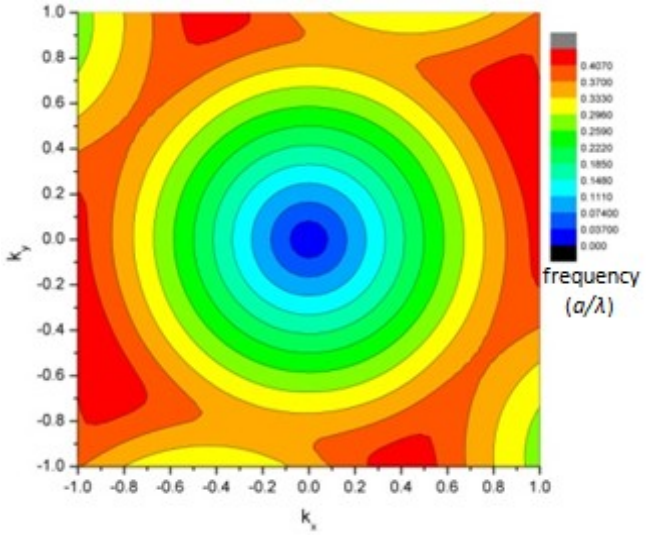
1.0
0.8
0.6
0.4
0.2
0.0
-0.2
-0.4
-0.6
-0.8
-1.0
k_y
-1.0 -0.8 -0.6 -0.4 -0.2 0.0 0.2 0.4 0.6 0.8 1.0
k_x
0.4070
0.3700
0.3330
0.2960
0.2590
0.2220
0.1850
0.1480
0.1110
0.07400
0.03700
0.000
frequency
(a/λ)

(c)

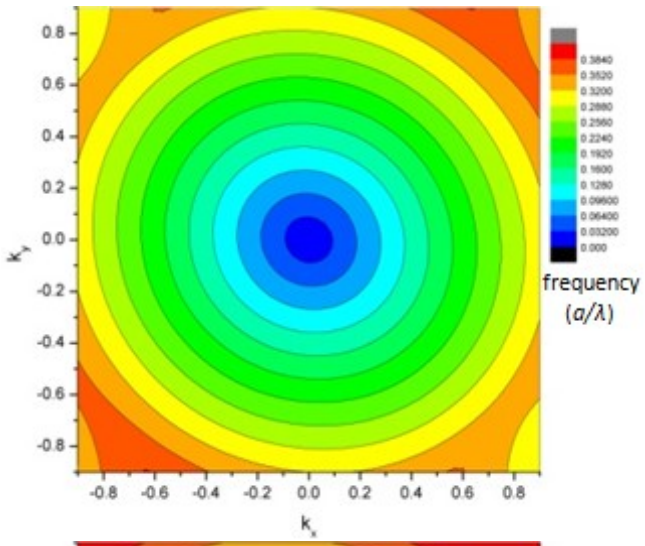
0.8
0.6
0.4
0.2
0.0
-0.2
-0.4
-0.6
-0.8
k_y
-0.8 -0.6 -0.4 -0.2 0.0 0.2 0.4 0.6 0.8
k_x
0.3840
0.3520
0.3200
0.2880
0.2560
0.2240
0.1920
0.1600
0.1280
0.09600
0.06400
0.03200
0.000
frequency
(a/λ)

(d)

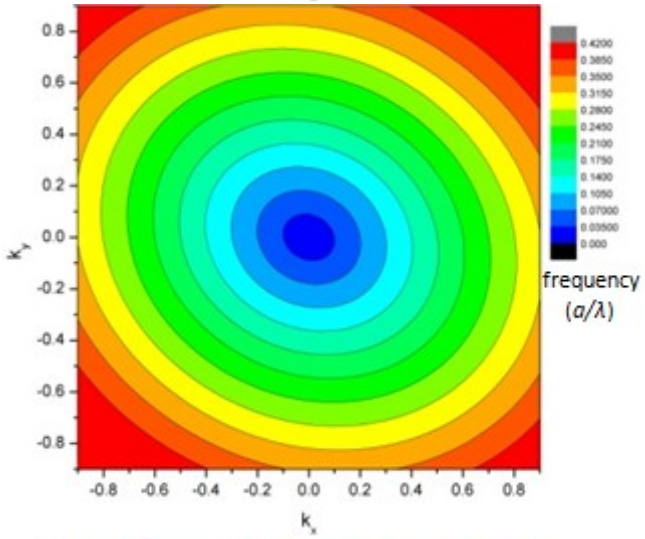
0.8
0.6
0.4
0.2
0.0
-0.2
-0.4
-0.6
-0.8
k_y
-0.8 -0.6 -0.4 -0.2 0.0 0.2 0.4 0.6 0.8
k_x
0.4200
0.3850
0.3500
0.3150
0.2800
0.2450
0.2100
0.1750
0.1400
0.1050
0.07000
0.03500
0.000
frequency
(a/λ)

(e)

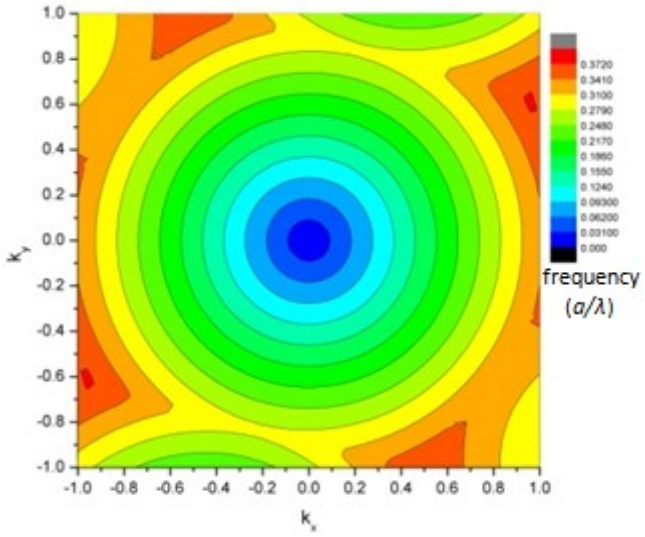
1.0
0.8
0.6
0.4
0.2
0.0
-0.2
-0.4
-0.6
-0.8
-1.0
k_y
-1.0 -0.8 -0.6 -0.4 -0.2 0.0 0.2 0.4 0.6 0.8 1.0
k_x
0.3720
0.3410
0.3100
0.2790
0.2480
0.2170
0.1860
0.1550
0.1240
0.09300
0.06200
0.03100
0.000
frequency
(a/λ)

(f)

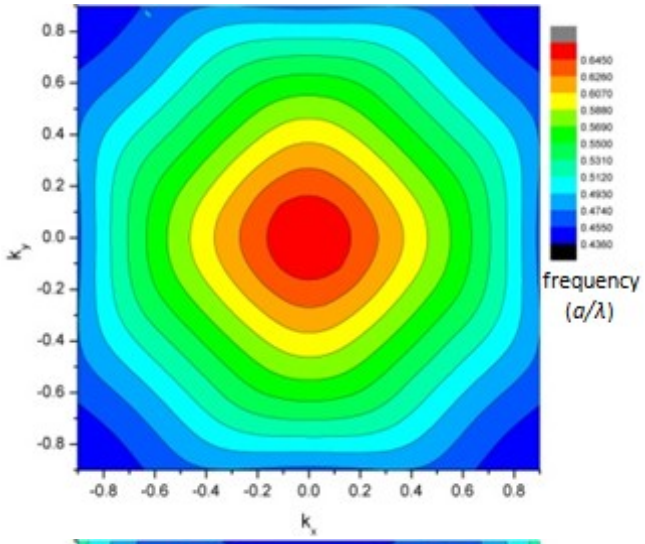
0.8
0.6
0.4
0.2
0.0
-0.2
-0.4
-0.6
-0.8
k_y
-0.8 -0.6 -0.4 -0.2 0.0 0.2 0.4 0.6 0.8
k_x
0.6450
0.6290
0.6070
0.5890
0.5690
0.5500
0.5310
0.5120
0.4930
0.4740
0.4550
0.4360
frequency
(a/λ)

(g)

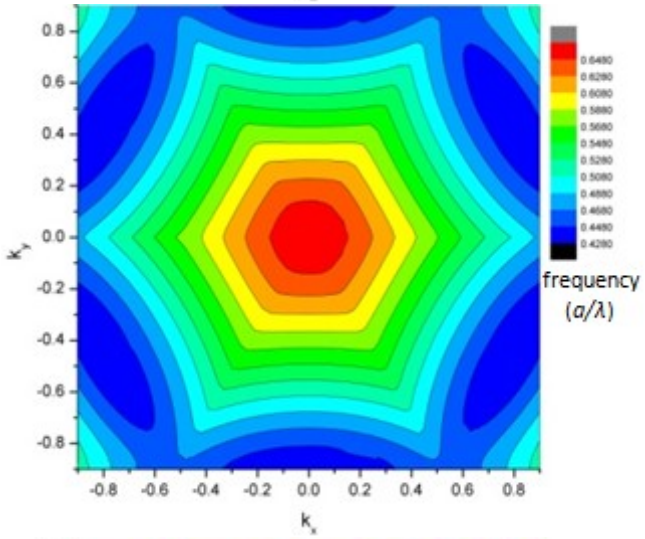
0.8
0.6
0.4
0.2
0.0
-0.2
-0.4
-0.6
-0.8
k_y
-0.8 -0.6 -0.4 -0.2 0.0 0.2 0.4 0.6 0.8
k_x
0.6480
0.6290
0.6080
0.5890
0.5680
0.5490
0.5290
0.5080
0.4890
0.4680
0.4490
0.4290
frequency
(a/λ)

(h)

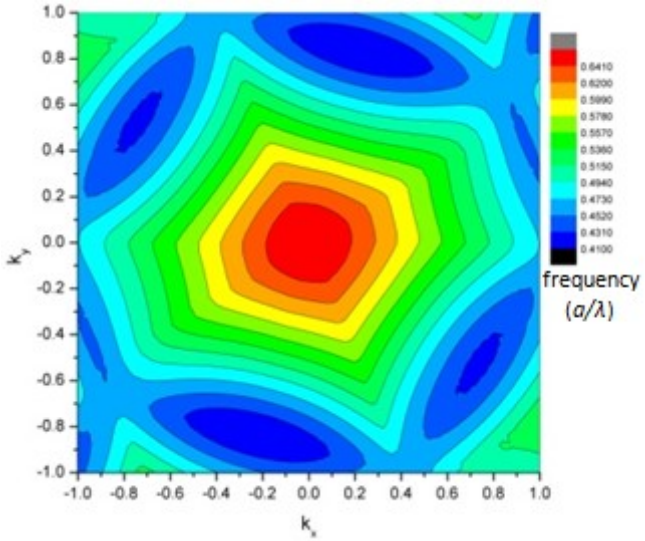
1.0
0.8
0.6
0.4
0.2
0.0
-0.2
-0.4
-0.6
-0.8
-1.0
k_y
-1.0 -0.8 -0.6 -0.4 -0.2 0.0 0.2 0.4 0.6 0.8 1.0
k_x
0.6410
0.6200
0.5990
0.5780
0.5570
0.5360
0.5150
0.4940
0.4730
0.4520
0.4310
0.4100
frequency
(a/λ)

(i)

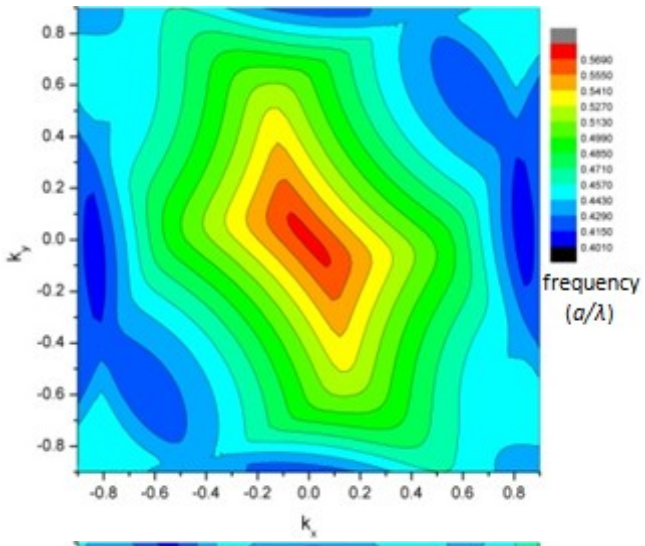
0.8
0.6
0.4
0.2
0.0
-0.2
-0.4
-0.6
-0.8
k_y
-0.8 -0.6 -0.4 -0.2 0.0 0.2 0.4 0.6 0.8
k_x
0.5690
0.5550
0.5410
0.5270
0.5130
0.4990
0.4850
0.4710
0.4570
0.4430
0.4290
0.4150
0.4010
frequency
(a/λ)

(j)

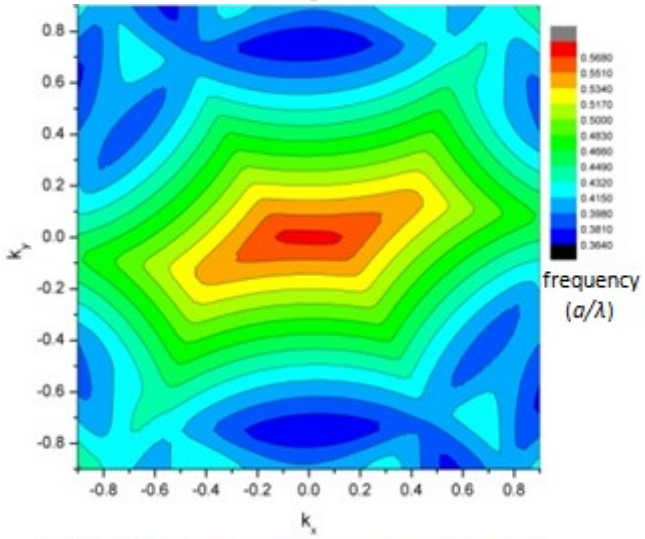
0.8
0.6
0.4
0.2
0.0
-0.2
-0.4
-0.6
-0.8
k_y
-0.8 -0.6 -0.4 -0.2 0.0 0.2 0.4 0.6 0.8
k_x
0.5680
0.5510
0.5340
0.5170
0.5000
0.4830
0.4660
0.4490
0.4320
0.4150
0.3980
0.3810
0.3640
frequency
(a/λ)

(k)

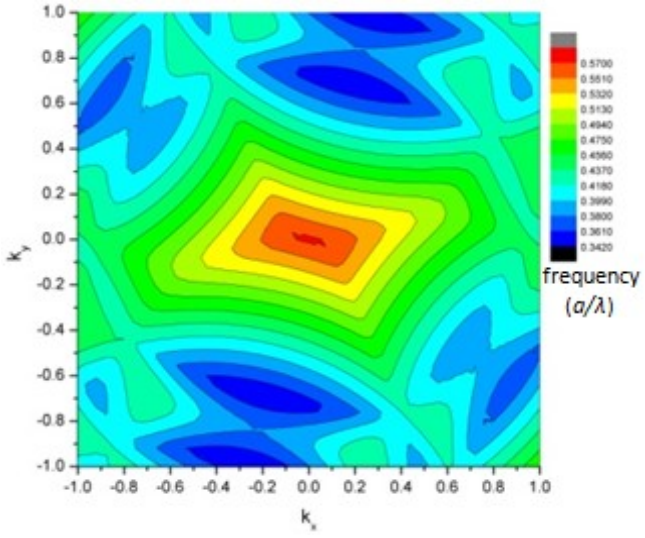
1.0
0.8
0.6
0.4
0.2
0.0
-0.2
-0.4
-0.6
-0.8
-1.0
k_y
-1.0 -0.8 -0.6 -0.4 -0.2 0.0 0.2 0.4 0.6 0.8 1.0
k_x
0.5700
0.5510
0.5320
0.5130
0.4940
0.4750
0.4560
0.4370
0.4180
0.3990
0.3800
0.3610
0.3420
frequency
(a/λ)

(l)

Figure 4.9 The EFCs are on cross section (100), (111), and (123), from left to right. External electric field is applied along the orientation of (123) with saturation strength. (a-c) untuned EFCs in the first band; (d-f) tuned in the first band; (g-i) untuned in the third band; (j-l) tuned in the third band.

The field direction could be arbitrarily chosen for the three-dimensional system. To study the directional tuning, electric field with saturation strength is applied along four different directions, (100), (110), (111), and (123), respectively. The results are shown in Fig. 4.10, featuring the EFSs of a normalized frequency 0.253 in the first band.

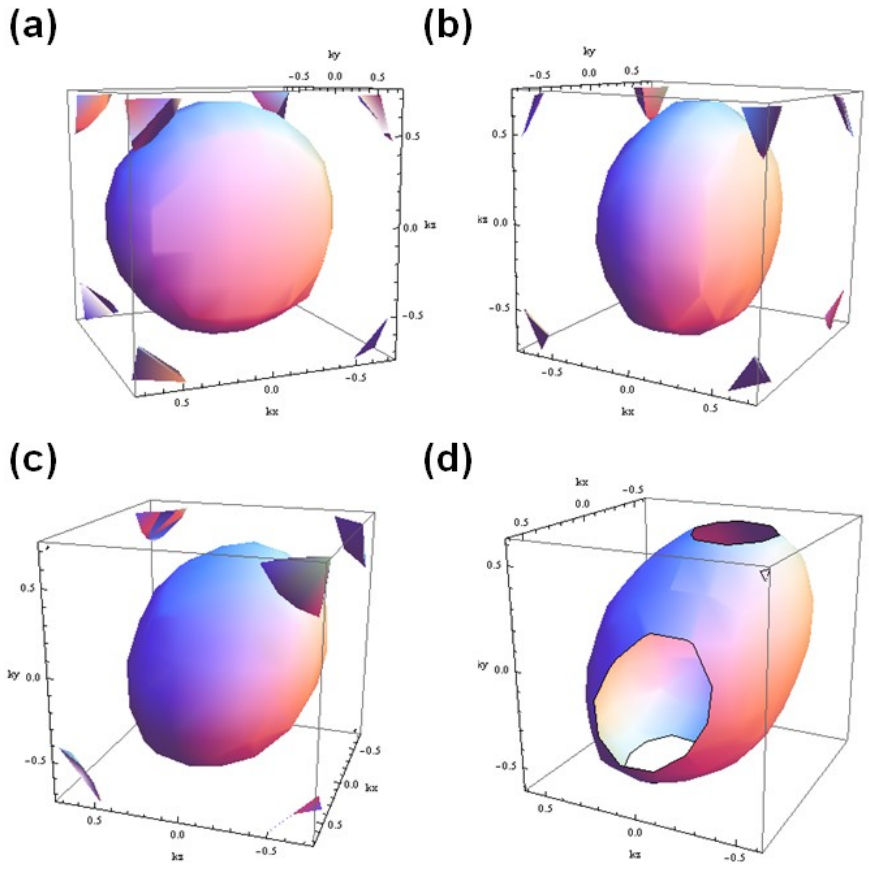

Figure 4.10 The EFS of frequency 2.53 in the first band with E field applied along different directions: (a) (100), (b) (110), (c) (111), and (d) (123).

The EFSs are compressed along the external field. These oblate-like surfaces share a similar shape, while following different orientations, providing a potential access to directing and switching the light beam.

References

[1] J. Langer, "Statistical theory of the decay of metastable states* 1," *Annals of Physics*, vol. 10, 1969.

[2] K. Ren, Z. Li, X. Ren, S. Feng, B. Cheng, and D. Zhang, "Three-dimensional light focusing in inverse opal photonic crystals," *Physical Review B*, vol. 75, 2007, pp. 1-6.

[3] C. Luo, S.G. Johnson, and J.D. Joannopoulos, "All-angle negative refraction in a three-dimensionally periodic photonic crystal," *Applied Physics Letters*, vol. 81, 2002, p. 2352.

[4] Z. Lu, S. Shi, J. Murakowski, G. Schneider, C. Schuetz, and D. Prather, "Experimental Demonstration of Self-Collimation inside a Three-Dimensional Photonic Crystal," *Physical Review Letters*, vol. 96, 2006, pp. 3-6.

[5] X. Chen, W. Jiang, J. Chen, and R.T. Chen, "Theoretical Study of Light Refraction in Three-Dimensional Photonic Crystals," *Journal of Lightwave Technology*, vol. 25, 2007, pp. 2469-2474.

[6] J. Joannopoulos, S. Johnson, J. Winn, and R. Meade, *Photonic crystals: molding the flow of light*, Princeton Univ Pr, 2008.

CHAPTER 5

CONCLUSIONS

5.1 Summary

This thesis summarizes works on the modeling and calculation of the PhCs featuring tunable anisotropic dielectric infill, trying to provide an insight into the photonic band structure and refraction properties, and to develop generalized analysis procedures.

Firstly, a PWE method based analysis is discussed. By solving the eigenvalue problem, band diagrams and EFCs (EFSs) were obtained in two- and three-dimensional structures, respectively. The refraction situation was thereby determined. A histogram calculation for DOS and LDOS was also developed from the PWE algorithm. The frequency resolution was determined both by the mesh fineness of the FBZ and the steepness of the gradient of EFCs (EFSs). To model the anisotropic nematic LC, the tensorial dielectric permittivity was taken into consideration. Coordinates rotation was introduced to simplify the mathematical process. The rotation transformation matrix is developed accordingly.

External field control of the LC-filled two-dimensional PhCs was studied in two categories, in-plane and off-plane tuning. A structure was designed based on the off-plane tuning to realize the switching among positive refraction, negative refraction and total reflection. The functionality was demonstrated in FDTD simulation. The in-plane tuning strongly alters the distribution of field density,

deforms the EFCs as well. The EFSs are presented. DOS and LDOS were calculated for comparison between tuned and untuned structures.

A method was developed to systematically analyze the propagation of EM waves in 3D PhCs. The PWE algorithm was employed to calculate the EFSs. The 3D analysis of light propagation was simplified into 2D problems by determining the incident plane and obtaining the in-plane dispersion relation. The out-of-plane refraction was discussed, based on which the positive and negative refractions were identified. As an example, negative refractions can be efficiently determined in any crystal structures and incident schemes. The deviation of light from the incident plane can also be precisely predicted in 3D PhCs.

5.2 Future work

The procedures could be readily applied to design and analyze PhC based devices. The goal is to include further investigation into potential applications, such as sensors, switchers, waveguides, etc. Beam shaping and direction control can be precisely predicted and accomplished. Particularly, the analysis in three dimensional PhCs can be largely facilitated by this study. There are still obstacles to be conquered for this purpose. The calculation resolution of EFSs and LDOS in 3D is astonishingly consuming. The PWE based procedure would take up around 6 hours to compute a 24×24×24 mesh, just for generating the eigen-frequencies to create the rough EFSs diagram. To include the field components for LDOS, with a decent resolution, days of computation are expected [1]. Another difficulty has

been met in the simulation of field distribution and beam propagation in 3D systems, which again is deemed an all consuming task. Distributed computing has shed some light on this task. The Beam tracing method also has its strength.

Reference

[1] I.S. Nikolaev, W.L. Vos, and A.F. Koenderink, "Accurate Calculation of the local density of optical strates in inverse-opal photonic crystals," *Journal of the Optical Society of America B*, vol. 26, 2009, p. 987.

Appendices

A. Calculation of photonic band diagram for 3D FCC structures using OptiFDTD7

PWE method has been successfully incorporated and can be accessed in many software packages. In this research, Optiwave OptiFDTD 7 is employed to provide a convenient tool for calculation of band diagrams, EFCs/EFSs and DOS for PBG structures. The general procedures are the same for the three tasks, either in 2D or 3D structures, except for the volume of the data and several steps in data processing. A calculation of band diagram in a FCC lattice will be described in this part.

A1. Create silicon spheres in a 3D FCC lattice in air background

Launch the "waveguide layout designer" module in the first place. Two constant materials are to be defined in the material management drop down menu. In this case, "air" ($\varepsilon = 1$) and "silicon" ($\varepsilon = 13$, i.e. $n = 3.6$) are specified.

In the project initial properties dialog box, define the wafer dimension as 5 μm×5 μm. Cladding and substrate layer are set to be 3 μm and 1 μm thick, respectively, with the materials both set as silicon.

In the layout designer, click on the *PBG Crystal Structure* icon, and place a lattice on the design plane. Define the lattice structure as FCC in the Crystal Lattice Properties dialog box (Fig. A.1), with scale set at 1 and number of lattice vectors

translation set as (#A, #B, #C) = (3, 3, 3). In the *Atom Waveguides in Unit Cell* box, add a new *True 3D Sphere Waveguide* at position (0, 0, 0). In the *Edit* tab, choose "silicon" for the material, and 0.353 for the radius.

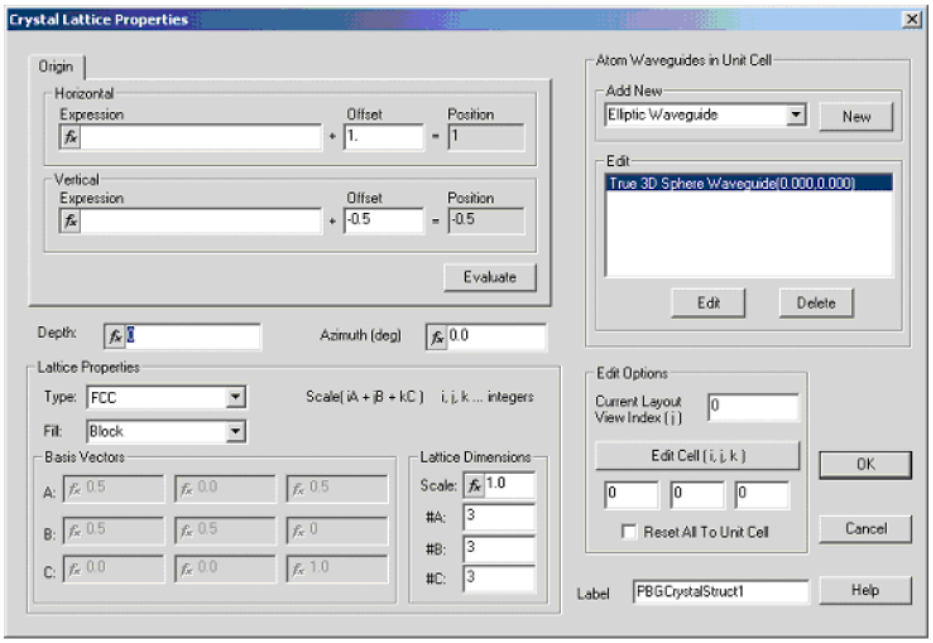

Figure A.1 Crystal lattice properties dialog box.

A2. Set PWE simulation parameters

Open PWE Simulation Parameters dialog box and set 3D solver as show in Fig. A.2. Hybrid polarization mode will be automatically selected. However, in 2D modes, the user can select either TE or TM mode. The base vectors are set by default. However, a more efficient choice is made by setting them as a = (0.5, 0, 0.5); b = (0, 0.5, 0) and c = (0.5, 0.5, 0). The default mesh size is set as 16×16×16. Usually the accuracy can meet requirements in most cases. It could be improved to set finer mesh.

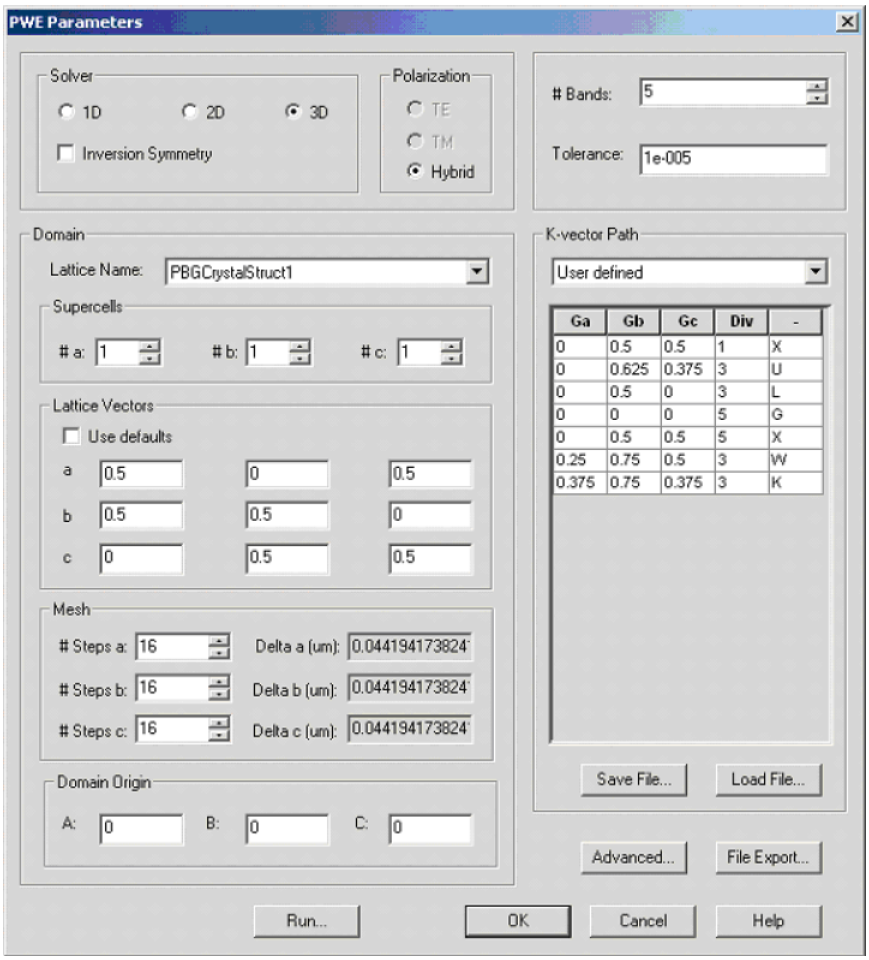

Figure A.2 PWE simulation parameters dialog box.

The ***k*** path in terms of reciprocal vectors is defined using the *User defined* in the *K-vector path* list. In this case, the FBZ is to be scanned. Definition of the high symmetry points is given in Fig. A.3.

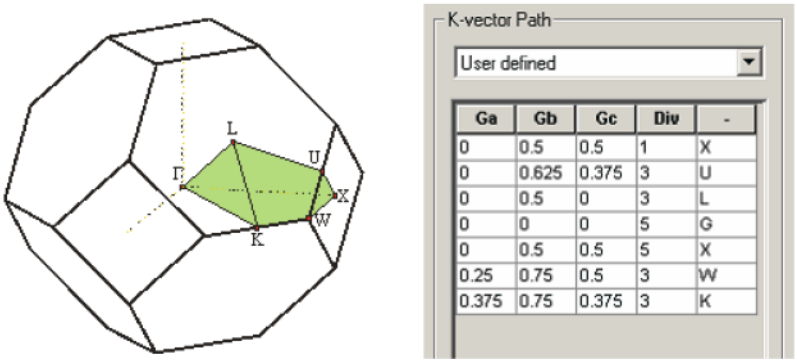

Figure A.3 Illustration of the FBZ of FCC structure with high symmetry points. To edit the ***k*** path, select "Add" in the *User defined* list to edit the terminal points and step size.

Add an input wave plane in the layout, and then perform the PWE band solver simulation. The resulting band structure does not contain any complete band gap (Fig. A.4). The output file is stored in ascii format, which could be readily retrieved by notepad or origin for post processing.

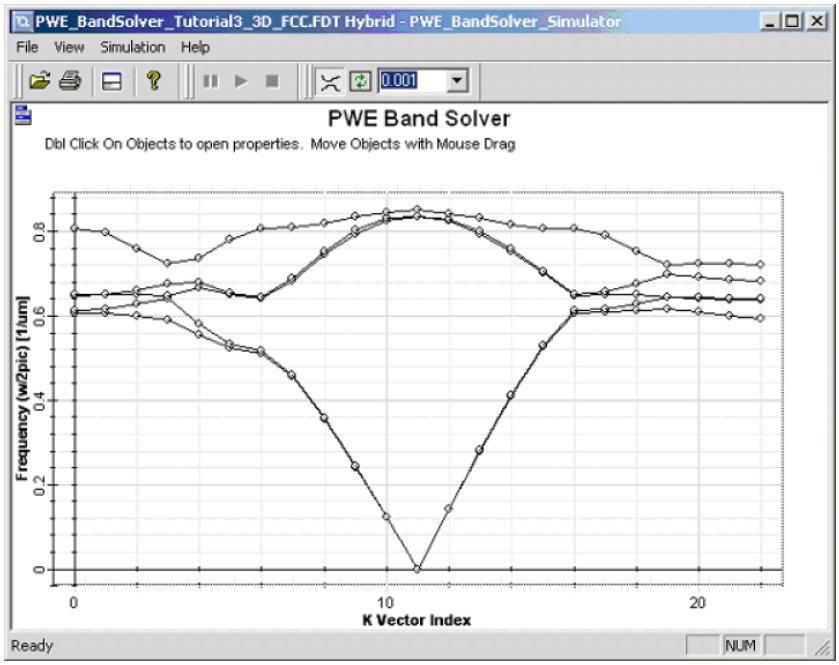

Figure A.4 Hybrid band structure of FCC lattice (mesh 16×16×16).

B. Generation of EFCs and EFSs

The generation of EFCs and EFSs are of the same procedure with that of band diagram in the calculation phase. The difference lies in the domain and number of data points sampled in the reciprocal space.

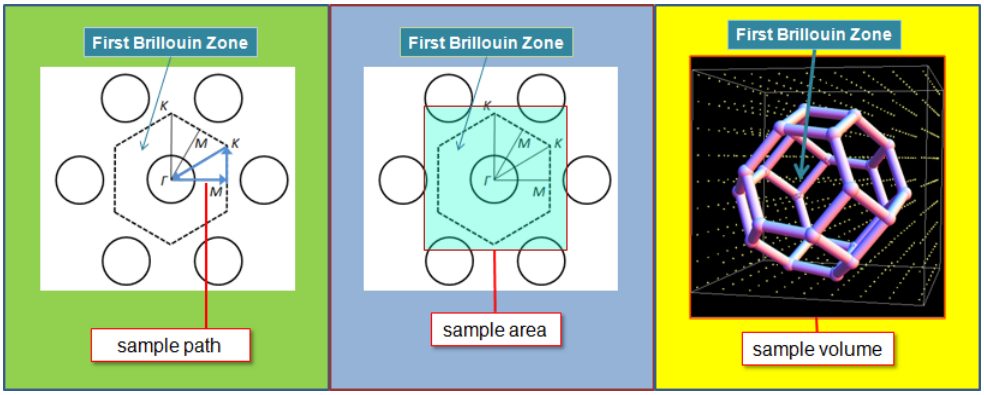

Figure B.1 Comparison of sampling domains in calculation of band diagram, EFCs in a two-dimensional structure and EFSs in a three-dimensional structure.

Considering the large array of points, their coordinates can be generated automatically using Mathworks Matlab 7 scripts.

For 2D Hexagonal lattice:

```
%%coordinates script for 2D
%%Definition of Hex lattice
T_Hex=[sqrt(3)/2 0.5;0 1 ];
delta=0.024;          %%Definition of mesh step size
n=0;
for j=1:51,
for i=1:51,             %% a 51×51 mesh
%%observer coordinates in reciprocal lattice
userx=-0.60+(i-1)*delta;
usery=-0.60+(j-1)*delta;
%%Transfer the user coordinates to the calculator
%%coordinates
temp=T_Hex*[ usery; userx];
n=n+1;
crd(n,1)=temp(1); %%calculator coordinates
crd(n,2)=0;
```

```
crd(n,3)=temp(2);
crd(n,4)=1;
crd(n,5)=n;
end
end
```

For 3D FCC lattice:

```
%%coordinates script for 3D
%%Definition of FCC lattice
T_FCC=[1/2 0 1/2;1/2 1/2 0;0 1/2 1/2];
delta=0.06;    %%Definition of mesh step size
steps=25;
n=0;
for k= -steps:steps,
for j=-steps:steps,
for i=-steps:steps,  %% a 25×25×25 mesh
%%observer coordinates in reciprocal lattice
Userx=i*delta;
Userx=j*delta;
Userx=k*delta;
%%Transfer the user coordinates to the calculator
%%coordinates
temp=T_FCC*[userx;usery;userz];
n=n+1;
%%the calculator coordinates
crd(n,1)=temp(1);
crd(n,2)=temp(2);
crd(n,3)=temp(3);
crd(n,4)=1;
crd(n,5)=n;
end
end
end
```

The generated list of coordinates is then fed into the *K-Vector Path* box in Fig. A.4. After running the calculation, the obtained data can be loaded into data processing software for analysis. The advantage of such software packages lies in their powerful built-in functions. In Mathworks Matlab 7.1, function **Contour**() and **Isosurface**() are readily employed to generate EFCs and EFSs, respectively. In OriginLab Origin 8.1, EFCs can be plotted directly from the drop down menu

in the *Plot* section. In Wolfram Mathematica 7, function **ListContourPlot**[] and **ListContourPlot3D**[] are designed for plotting EFCs and EFSs, respectively.

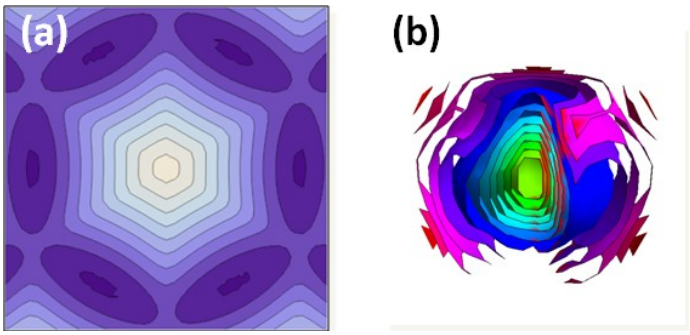

Figure B.2 (a) The second band EFCs generated by function **ListContourPlot**[] for a Hexagonal 2D PhC. (b) the first band EFSs visualized by function **ListContourPlot3D**[] for a FCC 3D PhC. Both processes were in implemented in Wolfram Mathematica 7.

Reference

[1] OptiFDTD Technical Background and tutorials, version 7.0, Optiwave, Inc.